REPORT

BIOLOGICAL MATERIALS

Coherently aligned nanoparticles within a biogenic single crystal: A biological prestressing strategy

Iryna Polishchuk,[1]* Avigail Aronhime Bracha,[1]* Leonid Bloch,[1]† Davide Levy,[1] Stas Kozachkevich,[1] Yael Etinger-Geller,[1] Yaron Kauffmann,[1] Manfred Burghammer,[2] Carlotta Giacobbe,[2] Julie Villanova,[2] Gordon Hendler,[3] Chang-Yu Sun,[4] Anthony J. Giuffre,[4] Matthew A. Marcus,[5] Lakshminath Kundanati,[6] Paul Zaslansky,[7] Nicola M. Pugno,[6,8,9] Pupa U. P. A. Gilbert,[4] Alex Katsman,[1] Boaz Pokroy[1]‡

In contrast to synthetic materials, materials produced by organisms are formed in ambient conditions and with a limited selection of elements. Nevertheless, living organisms reveal elegant strategies for achieving specific functions, ranging from skeletal support to mastication, from sensors and defensive tools to optical function. Using state-of-the-art characterization techniques, we present a biostrategy for strengthening and toughening the otherwise brittle calcite optical lenses found in the brittlestar *Ophiocoma wendtii*. This intriguing process uses coherent nanoprecipitates to induce compressive stresses on the host matrix, functionally resembling the Guinier–Preston zones known in classical metallurgy. We believe that these calcitic nanoparticles, being rich in magnesium, segregate during or just after transformation from amorphous to crystalline phase, similarly to segregation behavior from a supersaturated quenched alloy.

Diverse functional materials are formed in the course of biomineralization. They provide skeletal support (*1*), mastication (*2*), gravity sensing (*3*) and magnetic sensing (*4*), defense tools (*5*), photoreception (*6*, *7*), and more, using limited bioavailable elements. Natural processes for strengthening mineralized materials include the incorporation of intracrystalline macromolecules within their crystalline lattices, which increase the hardness and fracture toughness of the host crystals (*8*). A second strategy is the formation of structures with several orders of hierarchical architecture (*9*, *10*), shown to enhance the mechanical properties of the often-brittle building materials. A third strategy derives from transient amorphous precursor (*11*) from which many biominerals are formed, and which among other benefits facilitate the formation of curved and intricately shaped single crystals (*12*). A fourth finding is that biominerals often possess multifunctionality, allowing one material to exhibit several functions in parallel (*7*, *13*). Here we present another biostrategy, for toughening brittle single crystals of calcite.

Our studies of the atomic- and nanostructure of the dorsal arm plates of the brittlestar *Ophiocoma wendtii* (fig. S1) disclose the presence of coherent nanoprecipitates that induce comprehensive compressive stresses on the host single crystal, akin to the Guinier–Preston zones known in classical metallurgy (*14*). The arm plates of these brittlestars (*15*) are covered by hundreds of calcite lenses, each several tens of micrometers in size (*16*, *17*). The lenses were found to be part of a large single crystal, with microlenses that focus light onto photoreceptor nerve bundles positioned beneath them. Each lens is aligned along its optical axis parallel to the *c* axis of calcite. This orientation minimizes the effect of the birefringence of calcite, preventing double vision.

Lenses (Fig. 1A) have curved surfaces that focus light on the presumed photoreceptors (*16*, *17*). Examination of the dorsal arm plates by high-resolution powder x-ray diffraction (HRPXRD) (*15*) (Fig. 2A) revealed the structure of calcite only. After Rietveld refinement analysis, we obtained lattice parameters smaller than those of pure calcite, but very close in size to those expected from magnesium substitution (*18*): a = 4.92577(3) Å and c = 16.76897(6) Å (table S3). Measurement of the magnesium content and other impurities by means of inductively coupled plasma optical emission spectroscopy (ICP-OES), electron probe microanalysis (EPMA), and energy-dispersive spectroscopy (*15*) revealed an average concentration, η_{avg}, of about 15.2 ± 0.1 mol %, where η = Mg/(Ca + Mg) mol % (tables S1 and S2) (*15*). Magnesium readily substitutes for calcium in the calcite structure and causes the lattice parameters to shrink (*19*).

Typical bright-field aberration–corrected high-resolution transmission electron microscopy (HRTEM) images can be seen in Fig. 1, B and C. Even though the entire dorsal arm plate has been identified as a calcite single crystal, an ensemble of nanodomains can be observed within the matrix (Fig. 1, B and C). These nanodomains appear brighter in bright-field mode, indicating their relatively lower electron density. Despite the presence of these domains, fast Fourier transform (FFT) of the entire image on TEM yields a single-crystal pattern (Fig. 1, B and C, insets). On the likely assumption that the *O. wendtii* lenses are formed via transient amorphous precursors, as are other echinoderm ossicles (*11*), we explored the possibility that these nanodomains consist of residual amorphous material. This was ruled out, however, by differential scanning calorimetry coupled with thermal gravimetric analysis, which did not show any of the exothermal peaks (fig. S2) that are observed when amorphous calcium carbonate is heated and crystallized.

We further subjected powdered dorsal arm plates, while they were undergoing HRPXRD, to isochronous heating in situ at 30-min intervals at various temperatures up to 650°C. Upon heating, the diffraction peaks showed a large but gradual shift to lower diffraction angles (Fig. 2C) opposite in sign to that of the shift observed for other annealed biogenic calcites (*19*). After treatment at 650°C, the lens's lattice reverted to a calcite-like lattice with a median magnesium concentration of about 0.4 mol %. After annealing at 400°C, a new calcite nanoscale phase appeared, with lattice parameters a = 4.837(1) Å and c = 16.155(2) Å (Fig. 2C and table S3). The emergence of this nanophase was accompanied by a strong shift in peak position of the main calcite matrix. The lattice parameters of the calcite nanophase corresponded to a magnesium-rich phase with a magnesium concentration of η_p ~ 40 mol %. This nanophase is identical to that of the nanoparticles seen in the TEM imaging (Fig. 1, B to D), and their brighter appearance in bright-field TEM is explained by the presence of magnesium-rich calcite. Moreover, upon high-angle annular dark field (HAADF) scanning TEM, which provides *z*-contrast imaging, these nanodomains appear darker than the matrix, confirming a lower average atomic number, as expected for magnesium-rich particles in a calcium-rich matrix (fig. S3).

Samples were heated in situ within the TEM, which induced crystal growth. The nanoparticles grew from several nanometers to about 20 to 40 nm at 450°C (Fig. 1D). Line-profile analysis of

[1]Department of Materials Science and Engineering and the Russel Berrie Nanotechnology Institute, Technion-Israel Institute of Technology, 32000 Haifa, Israel. [2]The European Synchrotron, CS 40220, 38043 Grenoble Cedex 9, France. [3]Natural History Museum of Los Angeles County, Los Angeles, CA 90007, USA. [4]Departments of Physics, Chemistry, Geoscience, University of Wisconsin–Madison, Madison, WI 53706, USA. [5]Advanced Light Source, Lawrence Berkeley National Laboratory, Berkeley, CA 94720, USA. [6]Laboratory of Bio-Inspired and Graphene Nanomechanics, Department of Civil, Environmental and Mechanical Engineering, University of Trento, Via Mesiano 77, 38123 Trento, Italy. [7]Department for Restorative and Preventive Dentistry, Centrum für Zahn-, Mund- und Kieferheilkunde, Charité–Universitätsmedizin Berlin, 14197 Berlin, Germany. [8]School of Engineering and Materials Science, Queen Mary University of London, Mile End Road, London E1 4NS, UK. [9]Ket-Lab, Edoardo Amaldi Foundation, Italian Space Agency, Via del Politecnico snc, 00133 Rome, Italy. *These authors contributed equally to this work. †Present address: The European Synchrotron, CS 40220, 38043 Grenoble Cedex 9, France, and Institute of Technology in Zurich, Rämistrasse 101, 8092 Zürich, Switzerland.
‡Corresponding author. Email: bpokroy@technion.ac.il

the powder x-ray diffraction (XRD) corroborated this finding (fig. S4). Magnesium energy-filtered TEM of the heated sample confirmed that the domains were magnesium-rich when compared to the matrix (fig. S5). Proof that the domains are rich in magnesium was obtained, before heat treatment, by x-ray absorption near-edge structure spectroscopy and photoemission electron microscopy (XANES-PEEM) (*15*) (Fig. 3, A and B) and by two-dimensional (2D) time-of-flight secondary ion mass spectrometry (ToF-SIMS) (*15*) from a single lens (Fig. 3C). Both assessments revealed that the dispersed particles are richer in magnesium than the matrix. Component mapping with PEEM (*15*) was possible because the nanodomains and the lens matrix are spectroscopically distinct, as shown in XANES spectra (Fig. 3B and table S2).

As the calcite nanodomains are rich in magnesium, and the lattice parameters of these nanoparticles are considerably smaller than those of the calcite matrix, it would seem that at least part of the large shifts in diffraction peaks upon heating to larger lattice parameters is indicative of compressive strains in the crystal matrix. This is probably a result of coherence between the nanodomains and the matrix. The presence of local strain fields is confirmed by dark-field TEM imaging, in which strain fringes are seen (Fig. 1E); however, they completely disappear after heat treatment as the strains are relaxed (fig. S6).

We also performed submicrometer synchrotron scanning x-ray diffractometry (*15*) on cross sections of intact lens arrays, using a beam spot size of ~180 nm by 150 nm. Not only did this procedure verify that the entire lens array is a single crystal (see fig. S7), but we could also observe local variations of ±0.1% in the lattice parameters, as can be seen from the maps of the various *d* spacings (Fig. 4A).

The strengthening and toughening of these otherwise brittle lenses depends upon coherent magnesium-rich calcite nanoparticles within a lower-magnesium single crystal of calcite. These nanoparticles exert compressive strains on the matrix but are themselves under a high tensile strain. Because of the coherent interface before heat treatment, the presence of two distinct phases is not detectable on HRPXRD. However, if the diffractogram is plotted with the intensity in logarithmic scale, a hump can be observed at the base of each of the diffraction peaks before annealing (Fig. 2, A and B). Line-profile analysis yields a nanoparticle size of about 5 nm. As the sample is heated and the particles grow, the coherent interface is eventually destroyed. The nanoparticles are very similar to those in coherent Guinier–Preston zones of classical metallurgy, which are formed by rapid cooling of a homogeneous alloy, with limited solubility of one of the components at low temperatures. After quenching, the system is out of phase equilibrium and in a supersaturated solid solution state. As a result, and owing to the low rate of diffusion at ambient temperature, coherent nanoprecipitates form in the matrix in a process termed "aging" and exert strains.

We believe that the brittlestar lens demonstrates a very similar strategy. The $CaCO_3$–$MgCO_3$ binary phase diagram reveals limited solubility of Mg

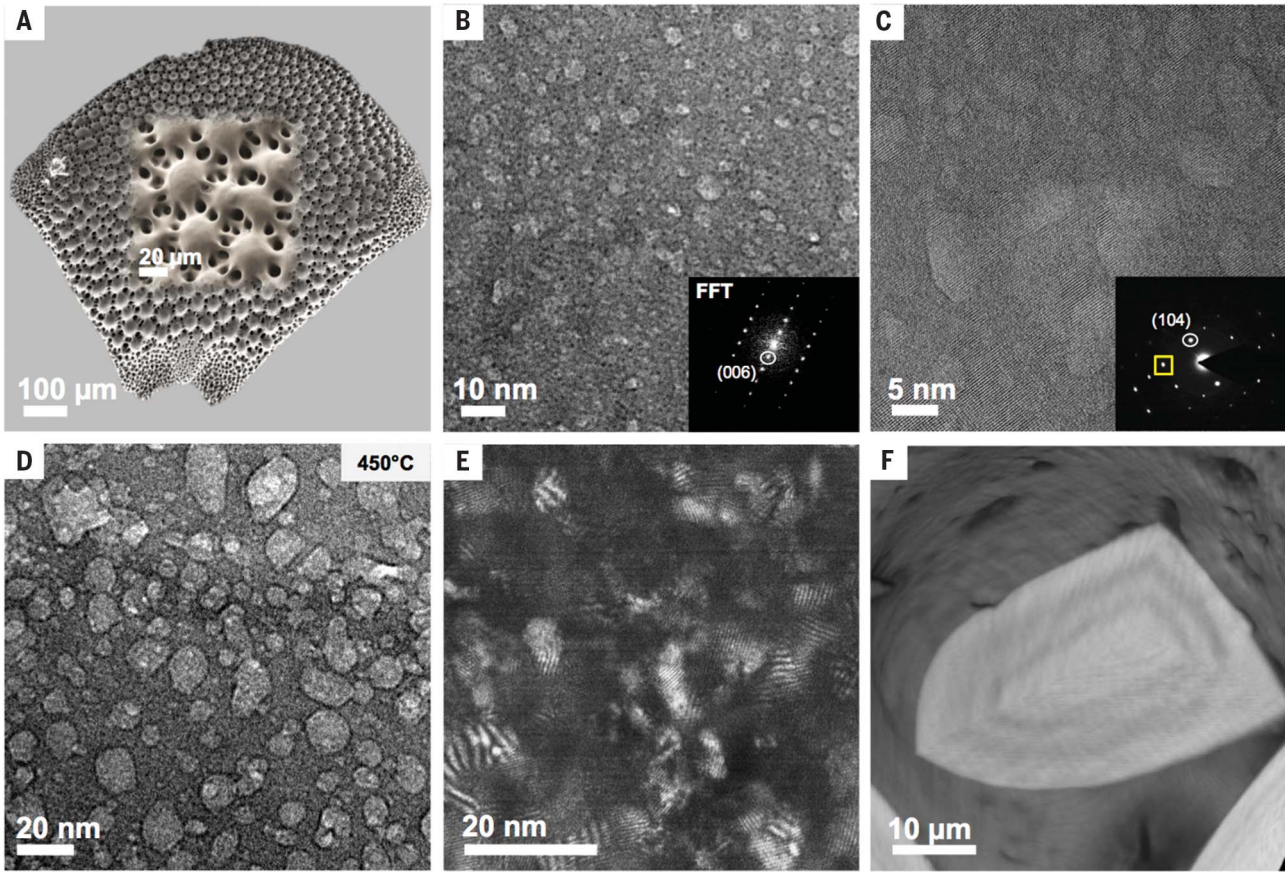

Fig. 1. Characterization from the micro- to the nanostructure. (**A**) Scanning electron microscopy image showing an entire dorsal arm plate and a higher-magnification inset. (**B**) HRTEM (*15*) image of a thin section from a lens revealing brighter nanodomains, although the FFT pattern (inset) is that of a single crystal. (**C**) Higher magnification of an area in (B) shows a lattice image undisrupted by the nanodomains, which demonstrate coherent interfaces with the lattice by the continuous lattice fringes. The inset shows an electron diffraction image from this area. (**D**) Bright-field TEM image obtained during in situ heating at 450°C, revealing the temperature-dependent growth of the nanodomains. (**E**) Dark-field HRTEM acquired using the diffracted beam marked by the diffraction spot in the yellow square in (C), and demonstrating numerous strain fringes. (**F**) A virtual slice within a single lens produced by 3D x-ray nanoCT (*15*), revealing alternating density layers probably owing to varying nanoprecipitate content.

(up to only a few Mg percent) in calcite at room temperature, after which dolomite is precipitated (*20*). It is reasonable to assume that the amorphous precursor is utilized in vivo as an alternative route to form supersaturated solid solutions (*11*), which allow for some precipitation of magnesium-rich calcium carbonate during or after crystallization.

Quantitative XRD data analysis of the heated samples reveals a volume fraction of ~8% magnesium-rich phase. This concentration may seem too low to exert coherent strains on the entire matrix; however, if we consider a simple case in which the precipitates are spherical with a radius of r_0, then the distance between particles, l, is determined by their volume fraction, ϕ: $l = r_0(4\pi/3)^{1/3}$. For ϕ = 0.06, the distance $l = 4r_0$ (see fig. S8) and the distance between particle is only $2r_0$. On the basis of TEM and XRD, we can estimate $2r_0$ to be ~5 nm. Bearing in mind that the strain caused by an isolated spherical coherent inclusion in the matrix decreases with distance according to the law $(r_0/r)^3$, the average strain of the matrix caused by the ensemble of coherent inclusions can be estimated as $3Z(q^3-1)^{-1}\ln q\Delta\varepsilon^c_{ij}$, where $\Delta\varepsilon^c_{ij}$ is the maximum coherent strain near the inclusion/matrix interface, $q = l/r_0$, and Z is the coordination number of a precipitate (we used Z = 6). If the precipitate volume fraction ϕ ~ 0.08, the average coherent strain of the matrix may reach a magnitude of ~$0.5\Delta\varepsilon^c_{ij}$. The average macroscopic strain in a stress-free bulk crystal containing a homogeneous distribution of coherent magnesium-rich inclusions is $\overline{\varepsilon_{kl}} = \varepsilon^0_{kl}\phi$, where ε^0_{kl} is the stress-free strain of the inclusion phase (transformation strain). This macroscopic strain consists of elastic and inelastic components. Inelastic strain caused by transformation strain of inclusions, ε^0_{kl}, can be accompanied by substantial internal coherent strains, with corresponding tensile stresses in the particles and compressive stresses in the matrix (*15*). Because of the small particle size, the particles can withstand relatively large tensile stresses against coherence loss. As known from metallurgical Guinier–Preston zones, the stresses arise owing to the presence of coherent interfaces (*21*). When a growing coherent inclusion reaches a certain critical size, the elastic energy becomes high enough to induce relaxation processes, and the coherence is lost (*21*). The nanoparticles' critical size for coherence loss is evaluated from 20 to 40 nm (*15*). This is shown in Fig. 2C, where the nanoparticles grow while at the same time, the strains in the particles (tensile) and in the matrix (compressive) are relaxed.

To estimate the absolute strain in the matrix, it is necessary to know the magnesium concentrations in both the matrix and the nanoparticles to derive their elastic constants and the difference in their lattice parameters that leads to the lattice mismatch. If we assume that for nanoparticles, ϕ = 8%, and that their composition is close to 40 mol % magnesium, this yields a matrix concentration of η_{matrix} = 13.3(1) mol % magnesium [$\eta_{avg} = \phi\eta_p + (1-\phi)\eta_{matrix}$]. Using a Mori-Tanaka homogenization scheme (*22*), we evaluated the average hydrostatic elastic strain within the nanoparticles as ~2.3% and within the matrix ~−0.1%. These coherent strains may result in an average compressive hydrostatic stress of ~−170 MPa in the matrix (*15*). At first glance, these figures appear to be high; however, if we consider the precipitate size to be ~5 nm, we can conclude that the strain state is very similar to that of a thin epitaxial layer that often contains misfits of this order even for calcium carbonate (*23*).

When the TEM imaging is observed from different orientations, the nanoprecipitates appear to have a platelet-like shape (fig. S9). This is confirmed by the small-angle x-ray scattering (SAXS) (*15*) signal that was derived from submicrometer scanning diffractometry and revealed streak-shaped signals, supporting the platelet-like shape. Notably, an orientation of the SAXS signal is seen only in certain distinct layers within a single lens, but as the curved surface is approached, a strongly oriented streaklike SAXS signal can indeed be observed, indicating that the platelets are oriented with their flat surfaces parallel to the lens surface (Fig. 4, B and C, and movie S1).

This alignment is most probably attributable to surface image forces known to affect precipitate orientation, because the coherence strains are much more readily relaxed at the free surface of a crystal than at its interior. In addition, SAXS reveals ordered regions slightly beneath the curved surface in curved lines parallel to the surface (Fig. 4B). The same images also reveal a zone of lower SAXS intensity closer to the surface (Fig. 4B, green-blue color). This zone resembles a precipitate depletion zone that could correspond to what is known in metallurgy as a precipitate-free zone (*24*). In the composition field, such segregation sets up a fluctuation that is perpendicular to the free surface and that develops to form alternating magnesium-rich and magnesium-depleted layers parallel to the surface, a phenomenon known as surface-directed spinodal decomposition (*25*, *26*). Notably, observation of the lattice parameter map from the same lens (Fig. 4A) reveals alternating lattice parameters that correspond to the features observed by SAXS (Fig. 4B).

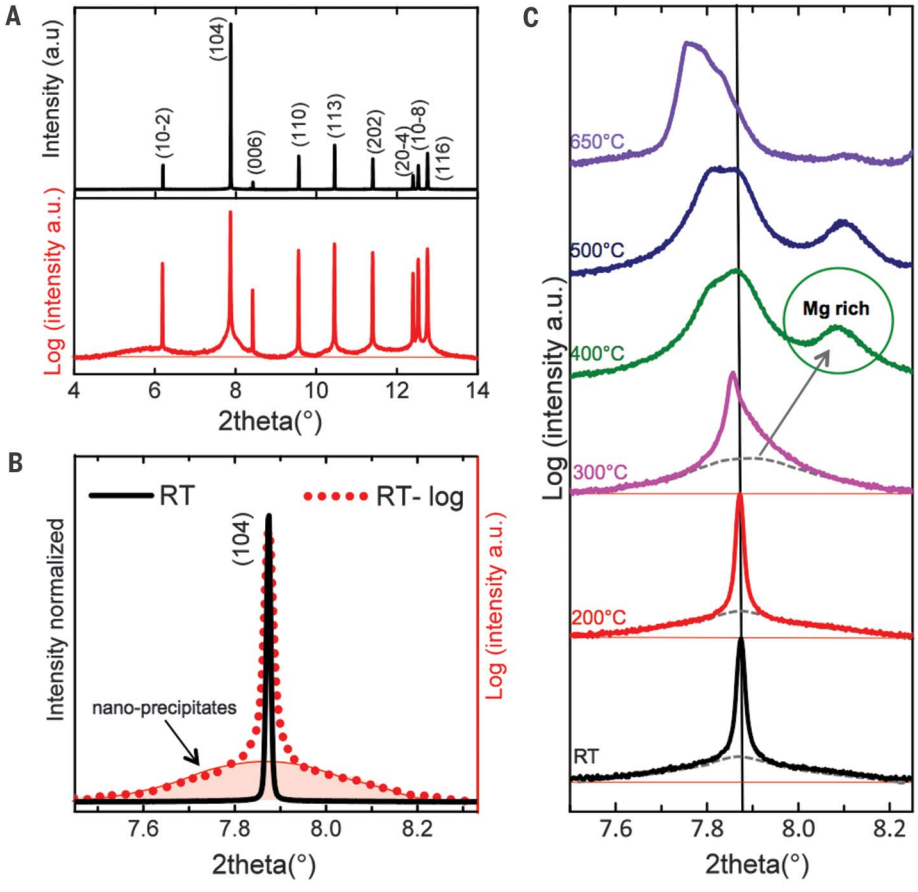

Fig. 2. High-resolution powder XRD characterization. (**A**) Full diffractogram of a powdered dorsal arm plates sample at room temperature collected at a wavelength of 0.4106 Å; linear intensity (black) and logarithmic intensity scales (red). (**B**) Enlargement of the (104) diffraction peak comparing linear (black) and logarithmic (red) intensity scales, and revealing the presence of nanodomains at the base of the diffraction peak. (**C**) Evolution of the (104) diffraction peak with heat treatments. After annealing at 400°C, a distinct broad diffraction peak appears owing to the heat-induced loss of nanoprecipitate coherence.

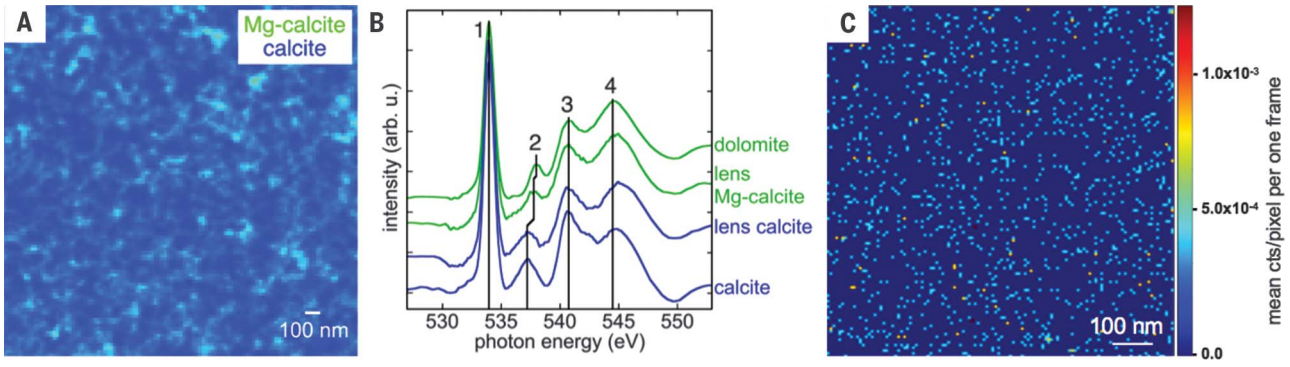

Fig. 3. PEEM and ToF-SIMS mapping. (**A**) PEEM component map with 20-nm pixels displaying the spatial distribution of the two phases in a brittlestar lens: low magnesium calcite (blue) and high magnesium calcite (green). Magnesium-rich calcite nanoparticles are only resolved as mixed with calcite (blue + green = cyan). (**B**) Oxygen XANES spectra show that lens calcite is similar to geological calcite, as shown by aligned peaks 1 to 4 (vertical lines, bottom). Lens Mg-calcite peak 2 is intermediate between calcite and dolomite. (**C**) Mg^+ distribution map acquired via ToF-SIMS analysis within a single lens. The map is 128 by 128 pixels, with 8 nm/pixel.

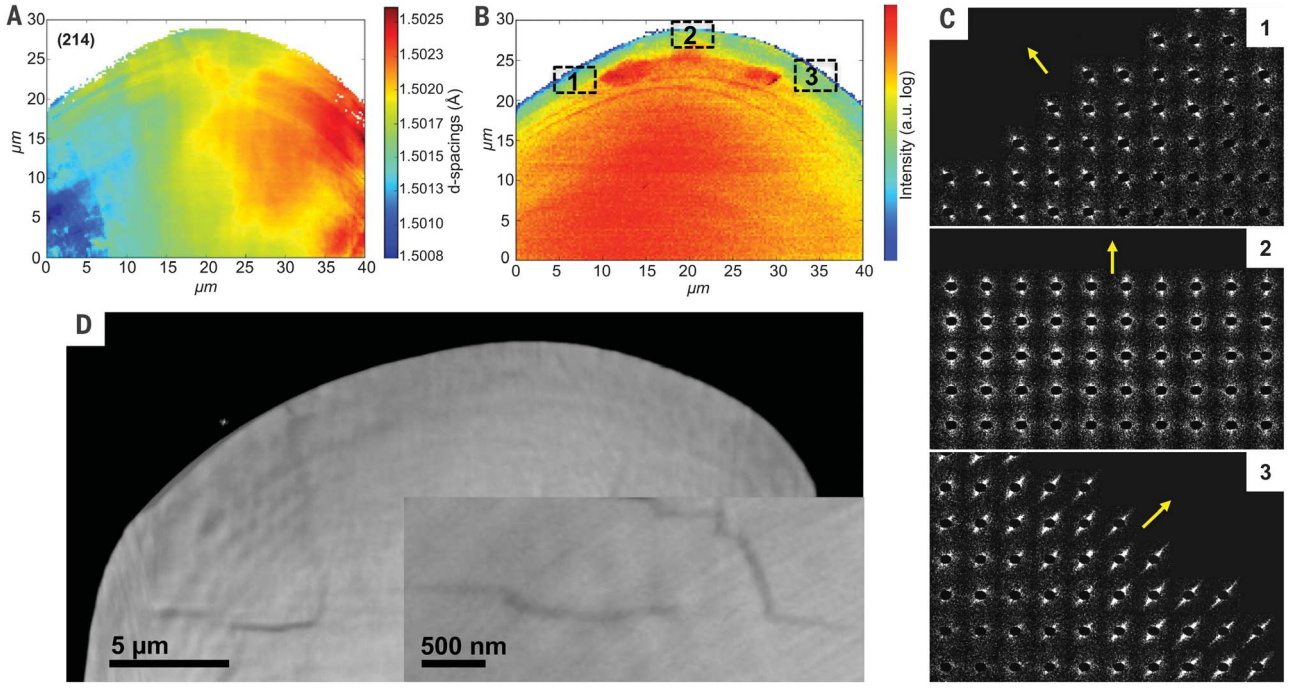

Fig. 4. Synchrotron submicrometer scanning diffraction and nanotomography. (**A**) A *d*-spacings map of a single lens area of the (214) reflection. (**B**) SAXS intensity map of the same lens (periodicities of ~2.5 to 16.5 nm). (**C**) SAXS signals from individual scanning positions reveal streaks elongated perpendicularly to the surface (yellow arrows). Numbering corresponds to the positions indicated in (B). (**D**) Nanotomographic map revealing alternating density layers. The inset (additional sample) shows a crack deflection resulting from the different density layers.

We performed indentation measurements and synchrotron nanotomography of a single lens after inducing cracks in it by mechanical cutting (*15*). From the indentation experiments, we could derive the values of the elastic constants and the hardness (table S4). To estimate the (mode I) fracture toughness K_{IC} of the samples, we used the classical Lawn, Evans, and Marshall model (*15*, *27*, *28*). Although this model was primarily developed for polycrystalline materials, the comparison of K_{IC} of various single crystals is possible. We performed the indentation measurements on the uppermost polished surface of the lenses, which corresponds to the [001] crystallographic direction of calcite, and hence we could compare our results to those obtained for [001]-cut and polished geological calcite. We found that the K_{IC} in brittlestar lens increased by more than twofold (2.21) relative to the geological counterpart, from 0.19 ± 0.06 to 0.42 ± 0.08 MPa·$m^{1/2}$ (table S5). These values are of the same order as those determined for geological calcite (*29*) (table S5), although the absolute values obtained in different studies cannot be rigorously compared. The indentation trace shows a layering structure, which is not observed in the geological counterpart (fig. S10) and is probably a result of cracks that propagate parallel to the alternating layers observed in Figs. 1F and 4, A, B, and D. Indentation on the heat-treated lenses (fig. S11) demonstrated that after annealing, the hardness (table S4) and the fracture toughness (table S5) decreased by 50 and 25%, respectively, as expected. The fracture toughness after annealing is nevertheless 1.63 times that of geological calcite.

Nano–computed tomography (nanoCT) of a single lens revealed that the lens has several alternating layers of density (indicated by the brightness in phase contrast in Figs. 1F and 4D).

The alternating densities are probably due to the different concentrations of magnesium-rich nanoprecipitates that coincide with the diffraction-mapping features. A varying density of nanoprecipitates results in varying degrees of compressive stresses in the lens, as indicated by the scanning diffractometry (Fig. 4, A and B). We would expect, then, a propagating crack to become more retarded and more deflected as the compressive stresses increase. Figure 4D (inset) shows that the crack indeed deflects each time it approaches a varying-density layer. Such crack deflection thus provides further evidence of enhanced toughness owing to the Guinier–Preston–like precipitates within the matrix; however, the layered structure can also contribute to the enhancement in mechanical properties (*30*). It should be emphasized that Guinier–Preston zones in metals lead to an increase in hardness, strength, and brittleness by mitigating dislocation motion, whereas in biogenic calcite, hardness, strength, and toughness are simultaneously enhanced by a different mechanism: namely, mitigation of cracks.

By considering the average crack deflection length $a_{=} = 300$ to 500 nm (along the layer interfaces of thickness $t \cong 250$ nm; see fig. S12) in combination with the measured compressive strain and calculated compressive stress $\sigma_0 \sim -170$ MPa in the matrix, we have developed a model to estimate the toughening $\frac{K^*_{IC}}{K_{IC}}$, resulting in

$$\frac{K^*_{IC}}{K_{IC}} = (1 - \sigma_0/\sigma_C)\sqrt{1 + ka_{=}/t}$$

where σ_C is the material strength in the absence of precompression and k represents the ratio between mode II and mode I fracture energies, assumed to be close to unity (*15*). From the measured toughening of the heated lenses (1.63, only due to crack deflection) and natural lenses (2.21, due to crack deflection and precompression), we estimate $a_{=} \sim 415$ nm (in agreement with the observations; see fig. S12) and $\sigma_C = 472$ MPa. Thus, the strength of the natural lenses $\sigma_C = \sigma_C - \sigma_0 = 642$ MPa demonstrates a strengthening only due to precompression of 1.36. The measured toughening of 2.21 and estimated strengthening of 1.36 represent a considerable simultaneous increase in both the fracture toughness and strength of calcite, the latter of which is typically on the order of a few tens of megapascals for macroscopic geological calcite (*31*).

Although there are some known examples of biogenic crystals under compression (*32*, *33*), the strategy described here provides an elegant way to maintain a solid matrix under compressive strains, known to be among the most efficient means of toughening ceramics such as tempered glass or prestressed concrete. The nanometric size of the precipitates enables them to bear the high tensile stresses. Another appealing aspect of this system is its ability to achieve a superior microstructure at ambient temperature and pressure as a result of its formation via supersaturated amorphous transient precursor rather than via heating and quenching, as in conventional materials science.

REFERENCES AND NOTES

1. A. H. Heuer *et al*., *Science* **255**, 1098–1105 (1992).
2. L. M. Gordon *et al*., *Science* **347**, 746–750 (2015).
3. J. A. Raven, A. H. Knoll, *Geomicrobiol. J.* **27**, 572–584 (2010).
4. R. Blakemore, *Science* **190**, 377–379 (1975).
5. J. C. Weaver *et al*., *Science* **336**, 1275–1280 (2012).
6. V. C. Sundar, A. D. Yablon, J. L. Grazul, M. Ilan, J. Aizenberg, *Nature* **424**, 899–900 (2003).
7. L. Li *et al*., *Science* **350**, 952–956 (2015).
8. A. Herman, L. Addadi, S. Weiner, *Nature* **331**, 546–548 (1988).
9. P. Fratzl, R. Weinkamer, *Prog. Mater. Sci.* **52**, 1263–1334 (2007).
10. A. R. Studart, *Adv. Funct. Mater.* **23**, 4423–4436 (2013).
11. E. Beniash, J. Aizenberg, L. Addadi, S. Weiner, *Proc. R. Soc. London Ser. B* **264**, 461–465 (1997).
12. Y. Politi, T. Arad, E. Klein, S. Weiner, L. Addadi, *Science* **306**, 1161–1164 (2004).
13. N. Vogel *et al*., *Proc. Natl. Acad. Sci. U.S.A.* **112**, 10845–10850 (2015).
14. O. B. M. Hardouin Duparc, *Metall. Mater. Trans. A Phys. Metall. Mater. Sci.* **41**, 1873–1882 (2010).
15. Materials and methods and supplementary text are available as supplementary materials.
16. J. Aizenberg, A. Tkachenko, S. Weiner, L. Addadi, G. Hendler, *Nature* **412**, 819–822 (2001).
17. G. Hendler, M. Byrne, *Zoomorphology* **107**, 261–272 (1987).
18. E. Zolotoyabko *et al*., *Cryst. Growth Des.* **10**, 1207–1214 (2010).
19. B. Pokroy *et al*., *J. Struct. Biol.* **155**, 96–103 (2006).
20. R. I. Harker, O. F. Tuttle, *Am. J. Sci.* **253**, 274–282 (1955).
21. P. Fratzl, O. Penrose, J. L. Lebowitz, *J. Stat. Phys.* **95**, 1429–1503 (1999).
22. T. Mori, K. Tanaka, *Acta Metall.* **21**, 571–574 (1973).
23. B. Pokroy, E. Zolotoyabko, *Chem. Commun. (Camb.)* **16**, 2140–2142 (2005).
24. P. N. T. Unwin, G. W. Lorimer, R. B. Nicholson, *Acta Metall.* **17**, 1363–1377 (1969).
25. S. M. Wise, J. S. Kim, W. C. Johnson, *Thin Solid Films* **473**, 151–163 (2005).
26. B. Aichmayer, P. Fratzl, S. Puri, G. Saller, *Phys. Rev. Lett.* **91**, 015701 (2003).
27. B. Lawn, R. Wilshaw, *J. Mater. Sci.* **10**, 1049–1081 (1975).
28. A. G. Evans, E. A. Charles, *J. Am. Ceram. Soc.* **59**, 371–372 (1976).
29. M. E. Kunitake, L. M. Mangano, J. M. Peloquin, S. P. Baker, L. A. Estroff, *Acta Biomater.* **9**, 5353–5359 (2013).
30. O. Kolednik, J. Predan, F. D. Fischer, P. Fratzl, *Adv. Funct. Mater.* **21**, 3634–3641 (2011).
31. D. Grady, R. Hollenbach, *Geophys. Res. Lett.* **6**, 73–76 (1979).
32. B. Pokroy, V. Demensky, E. Zolotoyabko, *Adv. Funct. Mater.* **19**, 1054–1059 (2009).
33. J. B. Forien *et al*., *Nano Lett.* **15**, 3729–3734 (2015).

ACKNOWLEDGMENTS

Helpful scientific discussions with P. Fratzl are acknowledged with thanks. We also thank M. Kalina for help in preparing the TEM samples and M. D'Incau and H. Gourkar (Anton-Paar Pvt. Ltd. India) for help during some of the microindentation experiments. The x-ray diffraction and nanoCT measurements described in this paper were carried out at beamlines ID13, ID22, and ID16B of the European Synchrotron Radiation Facility (Grenoble, France). This work was primarily supported by the Alon Fellowship for Outstanding Young Researchers of the Israeli Council for Higher Education (B.P.) and the RBNI Technion. N.M.P. is supported by the European Commission H2020 under the Graphene Flagship Core 1 no. 696656 (WP14 "Polymer Composites"), under the Future and Emerging Technologies Proactive "Neurofibres" no. 732344, and by Fondazione Caritro under "Self-Cleaning Glasses" no. 2016.0278 to L.K. P.U.P.A.G. acknowledges NSF grant DMR-1603192 and U.S. Department of Energy (DOE) grant DE-FG02-07ER15899. PEEM experiments were done at the Advanced Light Source, which is a DOE Office of Science User Facility supported by grant DE-AC02-05CH11231. The geological dolomite sample was provided courtesy of R. Slaughter (Univ. of Wisconsin, Geology Museum).

SUPPLEMENTARY MATERIALS

www.sciencemag.org/content/358/6368/1294/suppl/DC1
Materials and Methods
Supplementary Text
Figs. S1 to S12
Tables S1 to S5
Movie S1
References (*34*–*54*)

22 September 2016; resubmitted 16 March 2017
Accepted 27 September 2017
10.1126/science.aaj2156

Supplementary Materials for

Coherently aligned nanoparticles within a biogenic single crystal: A biological prestressing strategy

Iryna Polishchuk,* Avigail Aronhime Bracha,* Leonid Bloch, Davide Levy, Stas Kozachkevich, Yael Etinger-Geller, Yaron Kauffmann, Manfred Burghammer, Carlotta Giacobbe, Julie Villanova, Gordon Hendler, Chang-Yu Sun, Anthony J. Giuffre, Matthew A. Marcus, Lakshminath Kundanati, Paul Zaslansky, Nicola M. Pugno, Pupa U.P.A. Gilbert, Alex Katsman, Boaz Pokroy†

*These authors contributed equally to this work.
†Corresponding author. Email: bpokroy@tx.technion.ac.il

Published 8 December 2017, *Science* **358**, 1294 (2017)
DOI: 10.1126/science.aaj2156

This PDF file includes:

Materials and Methods
Supplementary Text
Figs. S1 to S12
Tables S1 to S5
Caption for Movie S1
References

Other Supplementary Materials for this manuscript include the following:
(available at www.sciencemag.org/content/358/6368/1294/suppl/DC1)

Movie S1

Materials and Methods

Sample Collection and Preparation

Ophiocoma wendtii were collected in Belize and preserved in 85% non-denatured ethanol prior to the experiments. Before any further measurements specimens were treated to remove tissue and other organic material from the surface of the skeleton, and to dissociate the ossicles and isolate individual dorsal arms plates. The arms of *Ophiocoma wendtii* were cut into segments and placed in a solution of deionized water (DI) and sodium hypochlorite (NaOCl, 10-15% solution), at varying concentrations and for various periods. Best results were obtained by submersion in a 2:1 concentration of NaOCl:DI water for 6 hrs. To avoid the dissolution of calcite samples 2% sodium carbonate Na_2CO_3 was added to all solutions.

Material Characterization

High Resolution Scanning Electron Microscopy (HRSEM). General SEM images for sample investigation were taken using a Zeiss Ultra-Plus FEG-SEM. A Schottky field emission gun scanning electron microscope with magnification ×12 to ×1,500,000; accelerating voltage, 200 V– 30 kV, and probe current 4 pA– 20 nA. Uncoated samples were imaged under a 1 keV beam current, otherwise charging would disrupt the imaging. Samples coated in carbon could withstand 5-10 keV without charging.

Focused Ion Beam (FIB) Microscopy. Thin transmission electron microscopy (TEM) samples were prepared with FEI Strata 400S Dual Beam system, a fully digital FEG-SEM equipped with FIB technology. Several samples were prepared: cross sections along horizontal direction of individual dorsal arm plate, cross sections along vertical direction, slices cut from powder samples.

Energy-Dispersive X-ray Spectroscopy (EDX). EDX measurements were conducted on the lens regions of dorsal arm plates with FEI E-SEM Quanta 200. Measurements were taken with a 20 keV beam, under a low vacuum of 0.3 Torr.

Electron Probe Micro-Analysis (EPMA). The analysis was done using a Cameca SX Five FE, in the Geoscience Department at the University of Wisconsin, Madison, after coating the reference dolomite samples with carbon, and the same *Ophiocoma wendtii* lenses analyzed in PEEM. We operated the instrument at 15kV and 10 nAmp, and defocusing the beam to 1 µm. Simulations showed 3-4 µm for Mg K_α lateral resolution, due to scattering and X-ray absorption for an assumed composition of $Mg_{0.25}Ca_{0.75}CO_3$. Simulations with 40nm and 500 nm beams gave identical results. The 1 µm beam used here also gave similar results, judging from the 4µm crater observed in the SEM micrographs after EPMA analysis in each spot. **Table S2** presents the data of EPMA analysis.

High Resolution Transmission and Energy Filtered Electron microscopy (HRTEM and EFTEM). TEM and STEM measurements were performed using an image C_s corrected FEI Titan 80-300 FEG-S/TEM system equipped with Gatan (Gatan Inc. Pleaseanton California) Tridiem 866 energy filter and coupled with a high-angle annular

dark-field imaging (HAADF) detector. Measurements were taken in several modes, including: bright field, dark field, phase contrast and diffraction contrast and at 300keV and 80keV to make sure that no beam damage occurs during the measurement.

High Resolution Powder Synchrotron Diffractometry (HRPXRD). The measurements were conducted at a dedicated beamline ID22 of the European Synchrotron Radiation Facility (ESRF, Grenoble, France) at a wavelength of 0.4106Å. This beam line uses a highly collimated and monochromatic beam to perform powder diffraction in the transmission setting. The beam passes through the sample and diffracts, to be collected on the opposite side by a set of 9 synchronized detectors, set 2.2° apart. The intensity of the diffractions is integrated over all detectors to produce high resolution diffraction patterns. Instrument calibration and wavelength refinement were performed with silicon standard NIST 640c.

For this analysis the samples were ground to a fine powder using an agate mortar and pestle. Powdered samples were loaded into borosilicate glass capillaries of diameter 0.7–1 mm. Isochronous annealing measurements were performed utilizing the X-ray diffractometer equipped with an in-situ heating system. Heating was done using a blower heater that blows hot air onto a very small area of the capillary, reaching a temperature resolution of 0.1°C. Heating locally ensures a precise temperature at the area where the X-ray beam collides with the sample and diffracts. Once the annealing time is up the blower heater was moved away while the capillary is spun around to allow quick and efficient cooling of the sample for a precise measurement. The samples were heated to a set of rising temperatures (200°C, 300°C, 400°C, 450°C, 500°C, 550°C, 600°C, and 650°C), annealed at each temperature for 30 minutes and then cooled down prior to recording a diffraction pattern.

Rietveld Method. The measured X-ray powder diffraction profiles were subjected to Rietveld refinement within the GSAS-II program (*34*). The analysis allowed determination of the lattice parameters, unit cell volumes and weight fractions of all the phases present in the investigated samples at different temperatures. Extracted values and goodness of fit parameters are summarized in **table S3**. Coherence length (nm) and micro-strain fluctuations along (104) plane of magnesium rich calcite nano-particles were derived applying the line profile analysis to (104) diffraction peak (**fig. S3**).

Coupled Differential Scanning Calorimetry-Thermogravimetric analysis (DSC-TGA) and Mass Spectrometry (MS). DSC/TGA measurements were performed using the LABSYS evo TGA/STA-EGA, and MS was performed using the Hiden QGA system. Measurements were taken with a reference crucible in an argon environment mixed with 20% air. Heating and cooling cycles were as follows: 1. Heating to 120°C and holding for ~ 30min to clear surface of sample from water molecules and contamination. 2. Heating to 650°C, at a rate of 5° min. 3. Cooling to ~ 40°C, at a rate of 5° min. and holding for ~ 30min to cool the sample completely. 4. Heating to 650°C, at a rate of 5° min. 5. Cooling to ~ 40°C, at a rate of 5° per min. Two heating cycles were executed in order to isolate processes that occur during heating and are irreversible. These processes would be seen in the first heating cycle but not the second.

Photoemission Electron Microscopy (PEEM). Data for the component maps and spectra (*35, 36*) of **Fig. 3A** and **3B** were acquired using PEEM-3, on beamline 11.0.1.1 at the Advanced Light Source (Lawrence Berkeley National Laboratory) and processed using the Gilbert Group Macros in Igor Pro ® (*37*). This type of mapping was previously done for Ca spectra (*38*). The spectral components used for the *Ophiocoma wendtii* lens map were: geologic dolomite (green) and *Ophiocoma wendtii* lens calcite (blue). The component maps were obtained enforcing positivity of the spectra, and allowing a ±0.45 eV shift of the entire spectra for best-fitting, and a background polynomial of second order. The spectra in **Fig. 3B** were obtained from averaging many single-pixels spectra, each obtained from a 20nm pixel. These were 226 Mg-calcite-rich pixels, and 217 calcite pixels from the *Ophiocoma* lens and 35 × 35=1225 pixels each from crystals of geologic dolomite and geologic calcite. All single-pixel spectra were first aligned in energy, then averaged, shifted in energy so that peak 1 was at 534 eV, and normalized so the intensities at the pre-edge and at the top of peaks 3 were 0 and 1, respectively, to obtain the spectra of **Fig. 3B**.

The geologic dolomite sample was a courtesy of Richard Slaughter, University of Wisconsin, Geology Museum. It originated from Black Rock, Arkansas. All samples for PEEM analysis were embedded in EpoFix (EMS, Hatfield, PA), and coated with 1nm Pt in the area of interest and 40 nm Pt around it, as described in ref. (*39*). The same samples were also used for EXAFS spectroscopies.

X-ray Absorption Fine Structure Spectroscopy (EXAFS). Calcium K-edge XAS was performed at three spots on one *Ophiocoma wendtii* lens at the beamline 10.3.2 of Advanced Light Source (Lawrence Berkeley National Laboratory) (*40*). The spectra were alike, so they were averaged together for analysis. Other XAS spectra were taken on an Mg-rich spot on the sea-urchin tooth, and also on the geologic calcite sample mounted in grazing-exit mode to reduce over-absorption (*41*). We used a simple model of the over-absorption effect to make the XANES spectra (*42*) of the lens (taken at 45°) match in peak height those of calcite. The EXAFS spectrum of calcite showed a strong peak at 3.7 Å in the Fourier transform from Ca-Ca pairs (6 Ca neighbors at 4.05 Å), whereas the lens spectrum showed only a weak peak at that position. We attempted to fit this peak with a mixture of Ca and Mg neighbors (using Artemis 0.8.014, from the IFEFFIT suite (*43*)), but the addition of Mg atoms did not result in improved fits over a model with Ca only, therefore the contribution of Mg neighbors was not detectable. What makes the 3.7 Å peak weak in the *Ophiocoma wendtii* lens is not the presence of Mg atoms, but a large increase in the second moment of the distance distribution ($\Delta\sigma^2$=0.05 Å² vs 0.01 Å² for calcite), which could be due to lattice distortions caused by the differing sizes of Mg and Ca cations. The average Ca-O distance was the same as in calcite to within 0.02 Å, but the second moment of the distance distribution of Ca-O is greater by 0.001-0.007 Å². We speculate that this dispersion in the Ca-O and Ca-(Ca,Mg) distances is related to the broadening of peak 2 observable in **Fig. 3B**.

Inductively Coupled Plasma Optical Emission Spectroscopy (ICP-OES). The system used was a Thermo Scientific Type iCAP6300 Duo ICP-OES. 3 mg of powdered samples were completely dissolved in 20µl of the 6M HCl solution, added to DI water to complete 10ml total for the analysis. During the experiment the sample is ionized by

currents created by electromagnetic induction, using time-varying magnetic fields. These ions emit light at wavelengths characteristic of a particular element, which are detected and analyzed. The emitted intensity is further correlated to the concentration of the element in the sample. The results of the measurements are presented in **table S1**.

Sub-Micron Scanning Synchrotron Diffractometry. Measurements were taken at the ID13 beamline, at the ESRF (Grenoble, France). A beam spot size used was approx. 180 nm × 150 nm at FWHM, with a wavelength of 0.832109 Å. The calibration of the instrument was performed on a standard corundum (Al_2O_3) powder sample,before and after the measurements. Both the calibration measurements were found to be in an excellent agreement with each other (~0.01% difference in the subsequent d-spacing calculations). The calculated effective distance between the sample and the detector was 12.9216 cm. Scans were made over several areas of the DAP, which include the lenses, and the underlying mesh structure. The sample was scanned at several angles, and to find the angles of maximal reflection intensities (*e.g.* for *d*-spacing calculations) angular intervals of 0.05° were used.

In order to recognize the useful areas (differentiate between the sample and the background) for each scan a mask was automatically generated, based on the intensity and the sharpness of the signal around the central spot. The parameters of recognition were kept constant for each series of measurements. The masked areas were ignored for all subsequent calculations.

Sample preparation included embedding the DAPs in EpofixTM Cold-Setting Embedding Resin and polishing from one side, using ÅngströmLap lapping films of 30, 15, 9, 3 and 1 μm grades. Then 1 mm thick Marienfeld microscopy glass slides were cut to about 1 cm × 1 cm squares, followed by drilling a 3 mm ⌀ hole in the center of each square. The polished sides of the epoxy-embedded samples were then glued onto the glass, so that the cross section of the DAP was positioned above the hole; in this way, the X-ray beam did not pass through the glass, which would cause unnecessary absorption. Lastly, the opposite side of the epoxy was cut and polished to obtain samples with a thickness of circa 50 μm.

Microindentation experiments. Microindentation tests were carried out to measure the Young's modulus, hardness and fracture toughness of the brittlestar lenses as well as of [001]-cut geological calcite (geocalcite) for comparison. Geocalcite sample did not require additional preparation as the surface was fairly smooth and flat enough to directly perform indentation experiments. For the lenses, the samples were embedded in a resin and polished using a series of 400, 800, 1200, 2000 and 4000 grade sand papers made of silicon carbide (HERMES). Finally, the samples were polished using a diamond paste with particle sizes in the range from 6 μm to 1 μm, to obtain a surface with minimal roughness. Poisson ratio of 0.31 was used for estimating the modulus. All the materials were indented using a standard CSM micro indenter with a load application of 100 mN. A standard Vickers indenter was used for measuring the properties of the material. The maximum applied load for indentation was chosen either by minimum detectable indentation impression visible through the microscope or a load that can make an indentation without resulting in catastrophic cracking of the sample surface.

The resulting experimentally obtained load-depth data were analysed using Matlab to determine the contact stiffness (S), reduced modulus (ER), and hardness (H) based on the well-established Oliver and Pharr method (*44*). The maximum displacement (hmax) at peak load (Pmax) and S were determined using the experimental data corresponding to the unloading curve. Specifically, S was defined as slope of the upper portion of the unloading curve during initial stages of unloading (*45*). We used the standard relation from Oliver-Pharr method to relate the measured stiffness to the reduced modulus given by

$$S = \frac{dP}{dh} = \frac{2}{\sqrt{\pi}} E_R \sqrt{A} \tag{1}$$

where A is the projected area of the contact between the indenter and the specimen. E_R is the reduced modulus defined using known parameters based on the modulus (E_i) and Poisson's ratio (υ_i) of the indenter. Thus,

$$\frac{1}{E_R} = \frac{(1-\nu^2)}{E} + \frac{(1-\nu_i^2)}{E_i} \tag{2}$$

The material hardness, *H*, is defined a

$$H = \frac{P_{max}}{A} \tag{3}$$

$$A = 26.43\, h_c^2 \tag{4}$$

where h_c is contact depth.

To estimate the fracture toughness K_{IC} of the samples we used the classical Lawn Evans Marshall model (*27*, *28*), i.e., $K_{IC} = \alpha \left(\frac{E}{H}\right)^{0.5} \left(\frac{P_{max}}{c^{3/2}}\right)$, where $\alpha = 0.016$, P_{max} is the indentation peak load, *E* is the elastic constant, *H* is the hardness and *c* is the crack length; *c* was determined as the largest crack taken from the center of the indentation impression to the crack tip, as specified in ref. (*28*) (fig. S10). Though this model was primarily developed for polycrystalline materials, the comparison of K_{IC} of various single crystals is possible. In the fracture toughness calculations, we used different elastic modulus and hardness values that correspond to geo-calcite and lenses, respectively. The estimated values of modulus and hardness of all the samples are reported in **table S4** and are compared with the only experimental data available in literature of the nanoindentation experiments that used Berkovich tip. The estimated fracture toughness for geocalcite and biocalciteis reported in **table S5**.

Nano-computed Tomography (nanoCT). Nanotomoraphy datasets were obtained on ID16B of the European Synchrotron Radiation Facility (ESRF, Grenoble France) (*46*) using phase contrast imaging based on holotomography (*47*). X-rays are focused down to a spot size of 50×50 nm^2 using two multilayer-coated Si mirrors in Kirkpatrick-Baez (KB) configuration under pink beam mode at 29.6 keV. The sample is positioned out of

the focal plane in projection geometry. While rotating the sample, 2001 high-resolution images are collected by a PCO camera with a pixel size of 25 nm. The datasets were processed using phase retrieval algorithm based on in-house software using the GNU Octave programming environment as described previously (*47*). Following reconstruction and cropping, different sample regions were visualized (*48*) to reveal the variable density layers in the lens as well as cracks propagating through the structure.

Time-of-Flight Secondary Ion Mass Spectrometry (ToF-SIMS). Measurements were performed utilizing LYRA3 FIB-SEM system (TESCAN, Czech Republic). Sample ionization is done by continual FIB/iFIB milling. Time of flight of the ions is measured with the TOFWERK detector (USA). Data visualized with the TESCAN 3D tomography tool. Sample was placed on standard aluminum holder with a conductive carbon tape. The LYRA microscope was used for this analysis. The Ga ions energy was 30 keV, ion beam current was 5 pA. ToF-SIMS analysis was performed in a positive ion mode. Analyzed area 1 x 1 μm^2.

Supplementary Text

Calculation of the Macroscopic Strain Induced by Homogeneous Distribution of Inclusions

The strain field of a macroscopically homogeneous distribution of inclusions can be found as a sum of the macroscopic (average) strain, $\overline{\varepsilon}_{ij}$, and the internal strain, $\Delta\varepsilon_{ij}(R)$, introduced by the internal displacement field with zero average gradient (*49*):

$$\varepsilon_{ij}(R) = \overline{\varepsilon}_{ij} + \Delta\varepsilon_{ij}(R) \tag{5}$$

An exact solution for internal strain can be found for a certain inclusion distribution with a given shape function, but this is not a subject of the present study.

The average macroscopic strain in a stress-free solid that contains a homogeneous distribution of inclusions is just the stress-free strain of the inclusion phase, ε_{kl}^0(called also as transformation strain), multiplied by its volume fraction, ϕ:

$$\overline{\varepsilon}_{kl} = \phi\,\varepsilon_{kl}^0 \tag{6}$$

For the case of magnesium calcite matrix containing magnesium-rich coherent nanoparticles, the stress-free strain in the particles can be calculated relative to the unstressed matrix. For example, for the sample with average magnesium concentration (cation mole fraction, η) of 15.2(1) mol%, magnesium concentration in the particles was found to be ~40 mol%, while in the matrix 13.3(1) mol%, that corresponds to the volume fraction of the particles $\phi \approx 0.08$. Lattice parameters of magnesium calcite (in Å) can be calculated using the relations (*18*):

$$\begin{aligned} a &= 4.98964 - 0.4287733\eta + 0.07308\eta^2 \\ c &= 17.06728 - 2.0291349\eta - 0.02223\eta^2 \end{aligned} \tag{7}$$

For the volume fraction of the particles ϕ, the non-zero macroscopic strain components can be calculated as:

$$\bar{\varepsilon}_{11} = \bar{\varepsilon}_{22} = \frac{a_p - a_m}{a_m}\phi, \qquad \bar{\varepsilon}_{33} = \frac{c_p - c_m}{c_m}\phi, \tag{8}$$

where the lattice parameters a_m and c_m correspond to the average magnesium concentration in the matrix, a_p and c_p are the lattice parameters of the nanoparticles. Using the values mentioned above one can find $\bar{\varepsilon}_{11} = \bar{\varepsilon}_{22} = -0.17\%$, $\bar{\varepsilon}_{33} = -0.26\%$ with average bulk contraction of $(\bar{\varepsilon}_{kk})/3 = -0.20\%$. The average strain is accompanied by an internal coherent strain, since the lattice parameters of the nanoparticles and the matrix change with opposite sign (matrix contracts and nanoparticles expand).

Average elastic strains in the matrix can be evaluated using a Mori-Tanaka homogenization scheme. Considering a matrix with homogeneously distributed inclusions and uniform elastic constants throughout a specimen, one can evaluate average elastic strain tensor in the matrix according to the expression (*22*):

$$\varepsilon_{ij}^{m} = -\phi\left(S_{ijmn}\varepsilon_{mn}^{0} - \varepsilon_{ij}^{0}\right) \tag{9}$$

where S_{ijmn} is the Eshelby's tensor. Using for ε_{mn}^{0} the values of the lattice mismatch corresponding to Mg concentrations in the matrix 13.3 mol.%, and in the nanoparticles 40 mol.%, one can find:

$$\varepsilon_{11}^{0} = \varepsilon_{22}^{0} = -0.02158, \qquad \varepsilon_{33}^{0} = -0.03249 \tag{10}$$

For hexagonal crystals, the Eshelby's tensor was calculated by Mura (*50*):

$$S_{ijmn} = \frac{1}{8\pi} C_{pqmn}\left(\bar{G}_{ipjq} + \bar{G}_{jpiq}\right) \tag{11}$$

where non-zero components of the $\bar{G}_{ijpq}$ are given below:

$$\bar{G}_{1111} = \bar{G}_{2222} = \frac{\pi}{2}\int_0^1 \Delta\left(1-x^2\right)\left\{\left[f\left(1-x^2\right)+h\rho^2x^2\right]\left[\left(3e+d\right)\left(1-x^2\right)+4f\rho^2x^2\right]-g^2\rho^2x^2\left(1-x^2\right)\right\}dx$$

$$\bar{G}_{1133}=\bar{G}_{2233}=2\pi\int_0^1\Delta\rho^2x^2\left(1-x^2\right)\left\{\left[(d+e)\left(1-x^2\right)+2f\rho^2x^2\right]\left[f\left(1-x^2\right)+h\rho^2x^2\right]-g^2\rho^2x^2\left(1-x^2\right)\right\}dx$$

$$\bar{G}_{1212}=\frac{\pi}{2}\int_0^1\Delta\left(1-x^2\right)^2\left\{g^2\rho^2x^2-(d-e)\left[f\left(1-x^2\right)+h\rho^2x^2\right]\right\}dx$$

$$\bar{G}_{1313}=\bar{G}_{2323}=-2\pi\int_0^1\Delta g\rho^2x^2\left(1-x^2\right)\left[e\left(1-x^2\right)+f\rho^2x^2\right]dx \qquad (12)$$

$$\bar{G}_{3333}=4\pi\int_0^1\Delta\rho^2x^2\left[d\left(1-x^2\right)+f\rho^2x^2\right]\left[e\left(1-x^2\right)+f\rho^2x^2\right]dx$$

$$\bar{G}_{3311}=\bar{G}_{3322}=2\pi\int_0^1\Delta\left(1-x^2\right)\left[d\left(1-x^2\right)+f\rho^2x^2\right]\left[e\left(1-x^2\right)+f\rho^2x^2\right]dx$$

where

$$\Delta^{-1}=\left[e\left(1-x^2\right)+f\rho^2x^2\right]\left\{\left[d\left(1-x^2\right)+f\rho^2x^2\right]\left[f\left(1-x^2\right)+h\rho^2x^2\right]-g^2\rho^2x^2\left(1-x^2\right)\right\},$$

ρ is the aspect ratio of the ellipsoidal inclusions, $d=C_{11}$, $e=\left(C_{11}-C_{12}\right)/2$, $f=C_{44}$, $g=C_{13}+C_{44}$, $h=C_{33}$. Using elastic moduli of calcite (*51*): $C_{11}=150GPa$, $C_{12}=58GPa$, $C_{13}=54GPa$, $C_{33}=85GPa$, $C_{44}=35GPa$, for spherical inclusions, $\rho=1$, from eqs. (11), (12) one can find the non-zero components of $\bar{G}_{ijpq}$: $\bar{G}_{1111}=0.057$, $\bar{G}_{1133}=0.094$, $\bar{G}_{3311}=0.116$, $\bar{G}_{3333}=0.094$, $\bar{G}_{1212}=-0.013$, $\bar{G}_{1313}=-0.02$, and the required components of the Eshelby's tensor: $S_{1111}=S_{2222}=0.537$, $S_{1122}=S_{2211}=0.024$, $S_{1133}=S_{2233}=0.056$, $S_{3311}=0.233$, $S_{3322}=0.076$, $S_{3333}=0.464$. Using equations (9) and transformation strains (8), one can find elastic strains in the matrix: $\varepsilon_{11}^m=\varepsilon_{22}^m=-6.1\cdot10^{-4}$, $\varepsilon_{33}^m=-8.6\cdot10^{-4}$, with compressive hydrostatic strain within the matrix $\varepsilon_H^m=-7\cdot10^{-4}$; corresponding compressive stresses in the matrix:

$$\sigma_{11}^m=\sigma_{22}^m=\left(C_{11}+C_{12}\right)\varepsilon_{11}^m+C_{13}\varepsilon_{33}^m\approx-180MPa \qquad (13)$$
$$\sigma_{33}^m=2C_{13}\varepsilon_{11}^m+C_{33}\varepsilon_{33}^m\approx-140MPa$$

and the hydrostatic compressive stress within the matrix $\sigma_H\approx-170MPa$. These values can be slightly different for elongated inclusions. For example, for $\rho=4$ and the same elastic constants, $\sigma_{11}^m=\sigma_{22}^m=205MPa$, $\sigma_{33}^m=53MPa$.

The Critical Size for Coherency Loss

The energy of a spherical coherent inclusion of phase α in the matrix of phase β is the sum of the elastic and surface energies:

$$\Delta E_{inclusion} = 4\pi R^2 \gamma_{coh} + \frac{4}{3}\pi R^3 \varpi \tag{14}$$

where γ_{coh} is the coherent interface energy, ϖ is the mean elastic energy per unit volume caused by the coherent inclusion (or distribution of coherent α-inclusions in the β-matrix).

The elastic energy per unit volume of the matrix caused by homogeneous distribution of similar coherent nanoparticles can be estimated using the following equation (*50*):

$$\varpi = -\frac{1}{2}\sigma_{ij}^{p}\varepsilon_{ij}^{T}\phi \tag{15}$$

where

$$\begin{aligned} \sigma_{11}^{p} &= \sigma_{22}^{p} = \left(C_{11} + C_{12}\right)\varepsilon_{11}^{p} + C_{13}\varepsilon_{33}^{p} \\ \sigma_{33}^{p} &= 2C_{13}\varepsilon_{11}^{p} + C_{33}\varepsilon_{33}^{p} \end{aligned} \tag{16}$$

are tensile stresses within the nanoparticles and ε_{ij}^{p} are the elastic strains within the nanoparticles (*22*):

$$\varepsilon_{ij}^{p} = \varepsilon_{ij}^{T}\phi - \varepsilon_{ij}^{T} = \varepsilon_{ij}^{T}\left(\phi - 1\right). \tag{17}$$

For the magnitudes of parameters found above, $\varepsilon_{11}^{p} = \varepsilon_{22}^{p} \approx 0.02$, $\varepsilon_{33}^{p} \approx 0.03$ with tensile hydrostatic strain within the nanoparticles $\varepsilon_{H}^{p} \approx 0.023$, tensile stresses $\sigma_{11}^{p} = \sigma_{22}^{p} \approx 5.74 Gpa$, $\sigma_{33}^{p} \approx 4.68 Gpa$ and $\varpi \approx 16 MJ/m^3$.

When a coherent inclusion reaches a certain critical size, the elastic energy becomes large enough to induce relaxation processes such as formation of misfit dislocations, the coherency is lost, and the elastic energy transforms to a new surface energy of incoherent inclusion/matrix interface with the energy γ_{incoh}. The critical size can be determined from the equation:

$$\bar{R} = \frac{3\left(\gamma_{incoh} - \gamma_{coh}\right)}{\varpi} \tag{18}$$

In order to evaluate this value, we need to know the interface energies (coherent and incoherent). If we assume reasonable values $\gamma_{incoh} = (0.1 \div 0.2)\ J/m^2$ and $\gamma_{coh} << \gamma_{incoh}$, then

$$\bar{R} \approx \frac{3\gamma_{incoh}}{\varpi} \approx (19-38)nm\,. \qquad (19)$$

This result corresponds well to the nanoparticles sizes observed during thermal treatment, when coherency is lost (TEM, XRD results).

Additional information on the XANES-PEEM experiment.

In **Fig. 3A** we present data obtained with PEEM demonstrating that Mg-calcite nanoparticles are interspersed and co-oriented with calcite in the *Ophiocoma wendtii* lens, but are spectroscopically distinct (**Fig. 3B**), thus their crystal and electronic structure differs from calcite. Notice that the peak 2 position in **Fig. 3B** for the *Ophiocoma wendtii* lens is intermediate between those of geologic calcite and dolomite. The precise peak positions are shown in **table S2**. This peak shift with Mg concentration in O spectra is observed here for the first time, but is consistent with Raman peak shifting with Mg concentration (*52*). This observation enables us to use the PEEM data to estimate the concentration of Mg in the Mg-rich calcite nanoparticles in the *Ophiocoma wendtii* lens, because the PEEM experiment only probes the next neighboring atoms to oxygen, and is different in the lens calcite matrix and the lens Mg-rich calcite nanoparticles (**Fig. 3B**). Specifically, the peak labeled 2 is due to O-Ca bonds or O-Mg, and disappears in simulated spectra of an artificial calcite structure in which all Ca atoms are replaced by Be (*42*).

Calculations of the Lattice Parameters in Accordance to Magnesium Content for High and Low Magnesium Calcite.

The relative concentration of magnesium, η, is calculated as follows:

$$\eta_{Mg} = \frac{C_{Mg}}{C_{Ca}+C_{Mg}}\,, \qquad (20)$$

where C_{Mg} and C_{Ca} are the molar fractions of Mg and Ca respectively.
The structural parameters of calcite containing certain amounts of magnesium could be calculated using Eq. 7 (*18*):

$$a = 4.98964 - 0.4287733\eta + 0.07308\eta^2$$

$$c = 17.06728 - 2.0291349\eta - 0.02223\eta^2$$

Calculations of the Magnesium Concentration based on the Results of ICP-OES Analysis.
Molecular weights used (numbers are given after subtracting reference data):

$$Mw_{Ca} = 40.078\frac{g}{mol}$$

$$Mw_{Mg} = 24.305\frac{g}{mol}$$

Number of *mols* was calculated using: $\#mol = \dfrac{wt\left[mg\right]}{Mw\left[\dfrac{g}{mol}\right]\cdot 1000\left[\dfrac{mg}{g}\right]}$

Number of CO_3 *mols* was calculated using: $mol_{CO_3} = 4\cdot\left(mol_{Ca} + mol_{Mg}\right)$

The *atomic* and *mol* percents of magnesium were calculated from the following expressions:

$$at\%_{Mg} = \frac{mol_{Mg}}{mol_{Ca} + mol_{Mg} + mol_{CO_3}}$$
$$mol\%_{Mg} = \frac{mol_{Mg}}{mol_{Ca} + mol_{Mg}} \qquad (21)$$

Detailed results of the ICP-OES analysis and calculated values of magnesium concentration presented in **table S1**.

Additional information on mechanical testing.

In this section, we present the simplest model able of predicting the toughening expected as a consequence of the two observed phenomena, i.e. of (i) matrix pre-compression and (ii) crack deflection at the layer-layer interface.

(i) In the case of a matrix pre-compression σ_0 ($\sigma_0 < 0$), the local stress-intensity factor at the tip of a crack will be given by $K_I^{(l)} = (\sigma_a + \sigma_0)\sqrt{\pi a}$ and the crack will propagate when $K_I^{(l)} = K_{IC} = \sigma_C\sqrt{\pi a}$, where K_{IC} is the fracture toughness, σ_a is the applied stress and σ_C is the stress at fracture in absence of pre-compression. This fracture criterion is equivalent to $K_I = \sigma_a\sqrt{\pi a} = K_{IC}^{(\sigma_0)} = K_{IC} - \sigma_0\sqrt{\pi a} = K_{IC}(1 - \sigma_0/\sigma_C)$, where K_I is the nominal (global) stress intensity factor and thus $K_{IC}^{(\sigma_0)}$ can be seen as the effective fracture toughness, as a consequence of the toughening due to the pre-compression. Similarly, the effective material tensile strength is $\sigma_C^{(\sigma_0)} = \sigma_C - \sigma_0$.

(ii) In the case of crack deflection at the layer-layer interface, the energy spent during crack propagation becomes higher due to an increment $a_=$ in the crack length along the interface. Denoting with G_{IC} the (nominal) mode I fracture energy (per unit area) and with G_{IIC} the (nominal) mode II fracture (i.e. interface adhesion) energy, the energy equivalence implies: $(G_{IC}a + G_{IIC}a_=)b = G_{IC}^{(a_=)}ab$, where $G_{IC}^{(a_=)}$ is the effective mode I fracture energy of the multilayered structure (and b is a width), as a consequence of the toughening due to the crack-deflection. From the classical correlation between fracture energy and toughness, i.e., $G_{IC} = K_{IC}^2/E$, we thus derive: $K_{IC}^{(a_=)} = K_{IC}\sqrt{1 + ka_=/a}$, where $k = G_{IIC}/G_{IC}$.

Combining the two mechanisms we finally find: $K_{IC}^* = K_{IC}(1 - \sigma_0/\sigma_C)\sqrt{1 + ka_=/a}$.

Noting that for the heat-treated lenses $\sigma_0 = 0$ (vanishing pre-compression) and assuming a plausible value for *k* close to unity the toughening is $\frac{K_{IC}^{(a_=)}}{K_{IC}} = \sqrt{1 + ka_=/a} = 1.63$ (see Table S5), we derive $\frac{a_=}{a} = 1.66$ and thus since a=t≅250nm is the mean thickness of the layers (see fig. S12) we deduce $a_=$≅415nm, in perfect agreement with the observations ($a_=$≅$300 - 500$nm) (see fig. S12).

For the natural lenses the observed toughening is $\frac{K_{IC}^*}{K_{IC}} = (1 - \sigma_0/\sigma_C)\sqrt{1 + ka_=/a} = 2.21$ (see Table S5, k=1) and thus for $\sqrt{1 + ka_=/a} = 1.63$ we derive $1 - \sigma_0/\sigma_C = 1.36$; considering σ_0≅ −170MPa, as we have estimated according to the Mori-Tanaka model (and confirmed with an experimental-theoretical independent model), we deduce $\sigma_C =$ 472MPa and thus $\sigma_C^{(\sigma_0)} = \sigma_C - \sigma_0 = 642$MPa.

Fig. S1.

Photograph of *Ophiocoma wendtii.*

Preserved specimen of *Ophiocoma wendtii* from the Echinoderm Collection of the Natural History Museum of Los Angeles County.

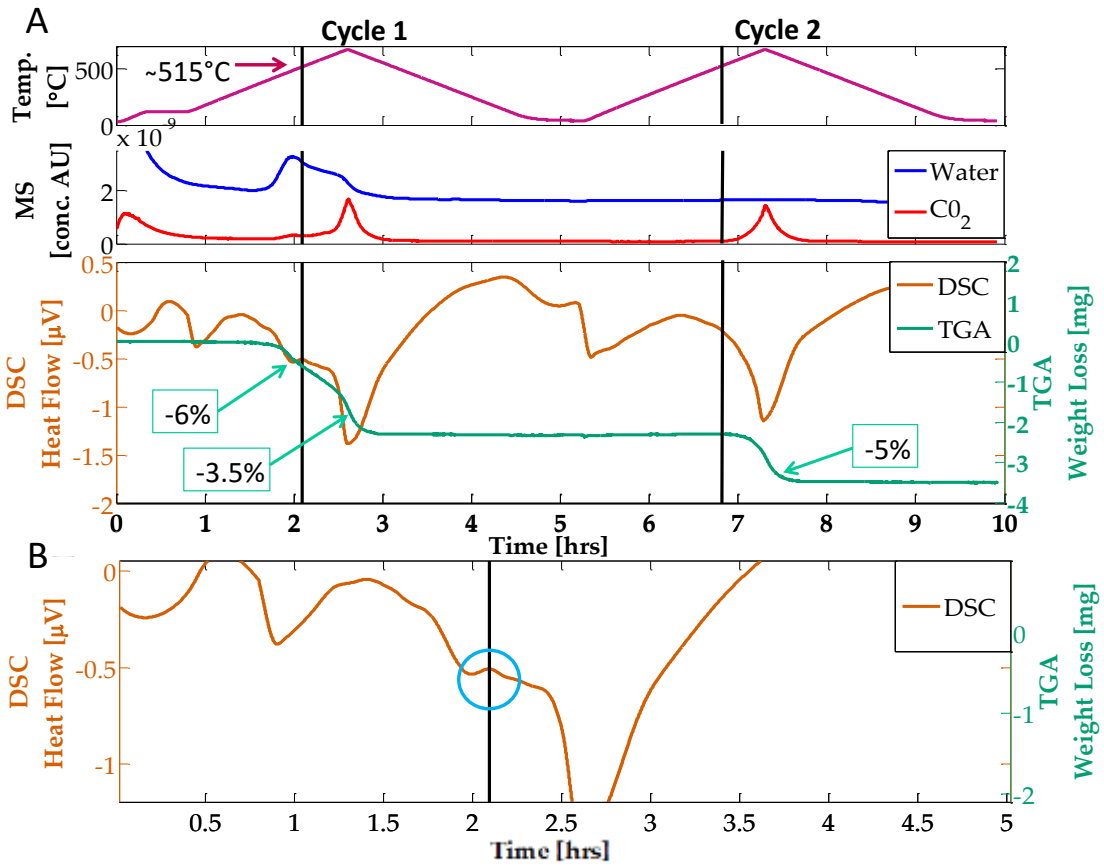

Fig. S2.

Results of coupled DSC, TGA and MS measurements for water and CO_2.
(A) Complete measurement done in two heating cycles. Vertical lines are at the position of 515°C, where a small peak can be seen in the DSC results. Percent numbers marked denote the amount of material lost during heating in TGA measurement. (B) Zoom in on the mentioned peak at 515°C. The peak although detectable, is far too small to indicate an amorphous-to-crystalline transformation.

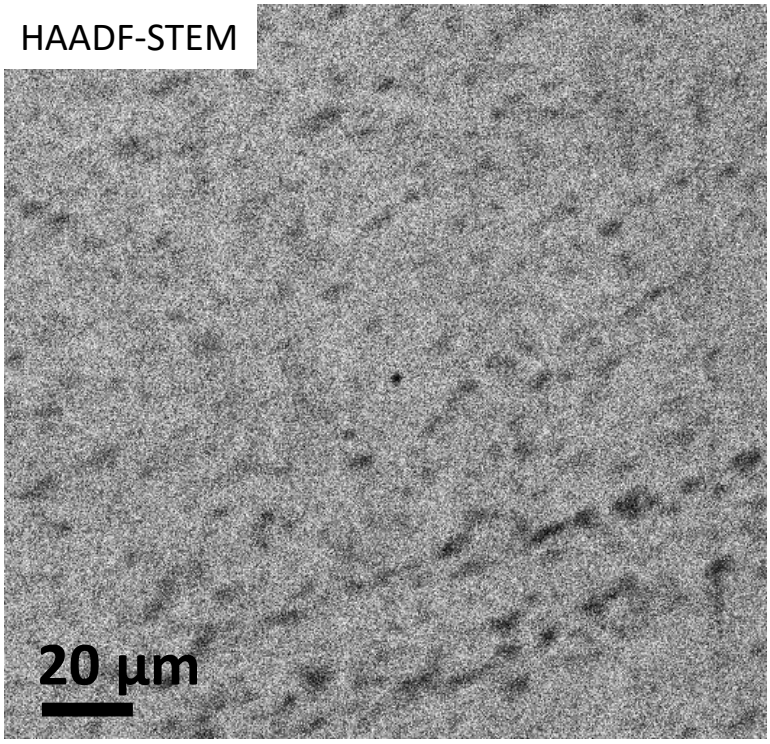

Fig. S3.

High angle annular dark-field scanning transmission electron microscope (HAADF-STEM) image of a section from a lens.

This method provides z-contrast imaging. As can be seen the nanodomains appear darker than suronding matrix confirming an average lower atomic number as expected for magnesium-rich particles in a calcium-rich matrix.

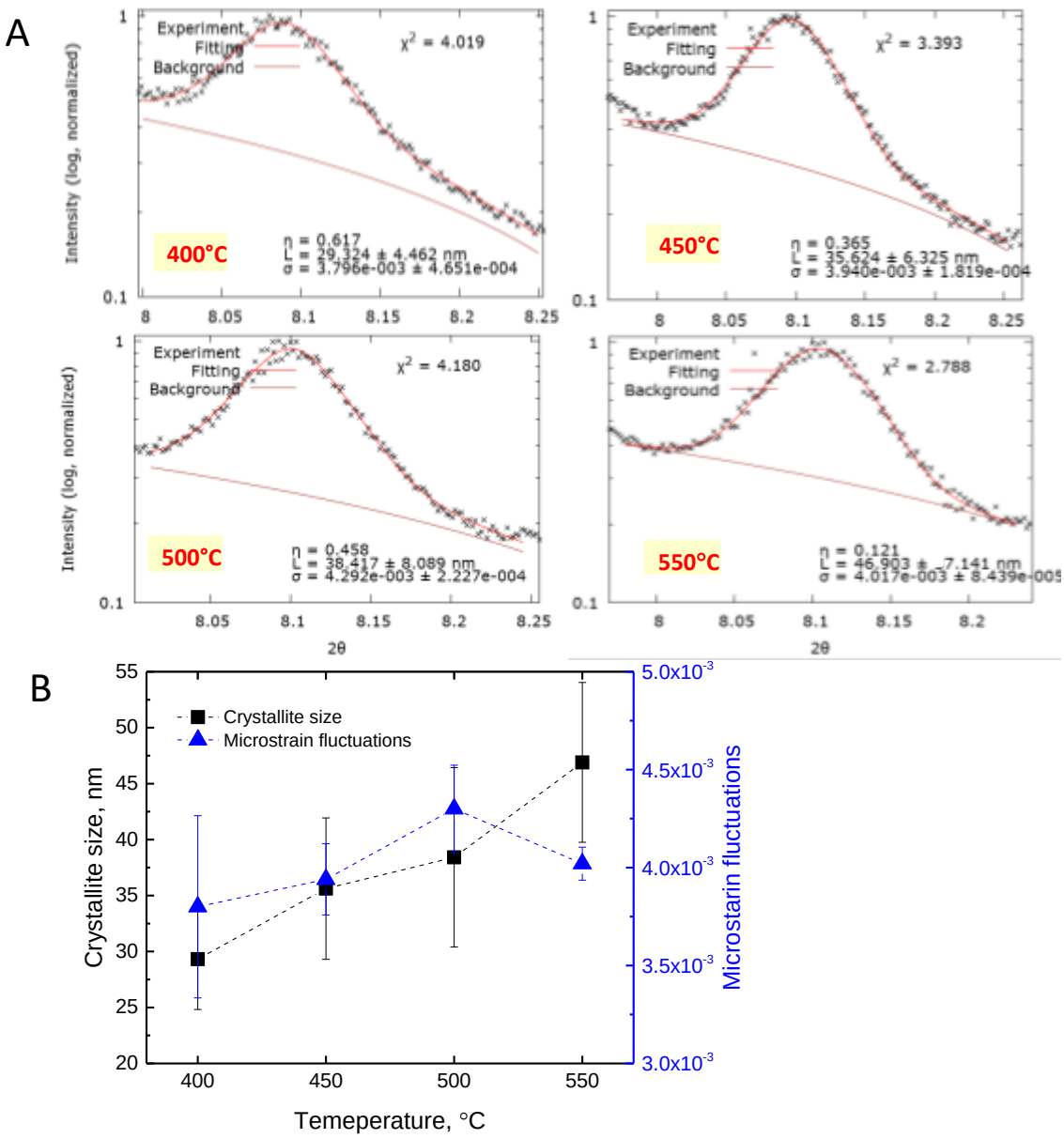

Fig. S4.
XRD line profile analysis of the (104) plane of the magnesium-rich phase.
(A) Microstructural evolution of the (104) plane in calcite nanodomains subjected to thermal annealing. In order to determine the Lorentzian (crystallite size) and Gaussian (micro-strain fluctuations) contributions on a single diffraction peak we applied the Voigt function approach (*53*). The profile fitting was performed utilizing the Gnuplot 5.0 interface (*54*). (B) Obtained results demonstrate an increase in crystallite size upon annealing accompanied by the increase in the averaged micro-strain fluctuations.

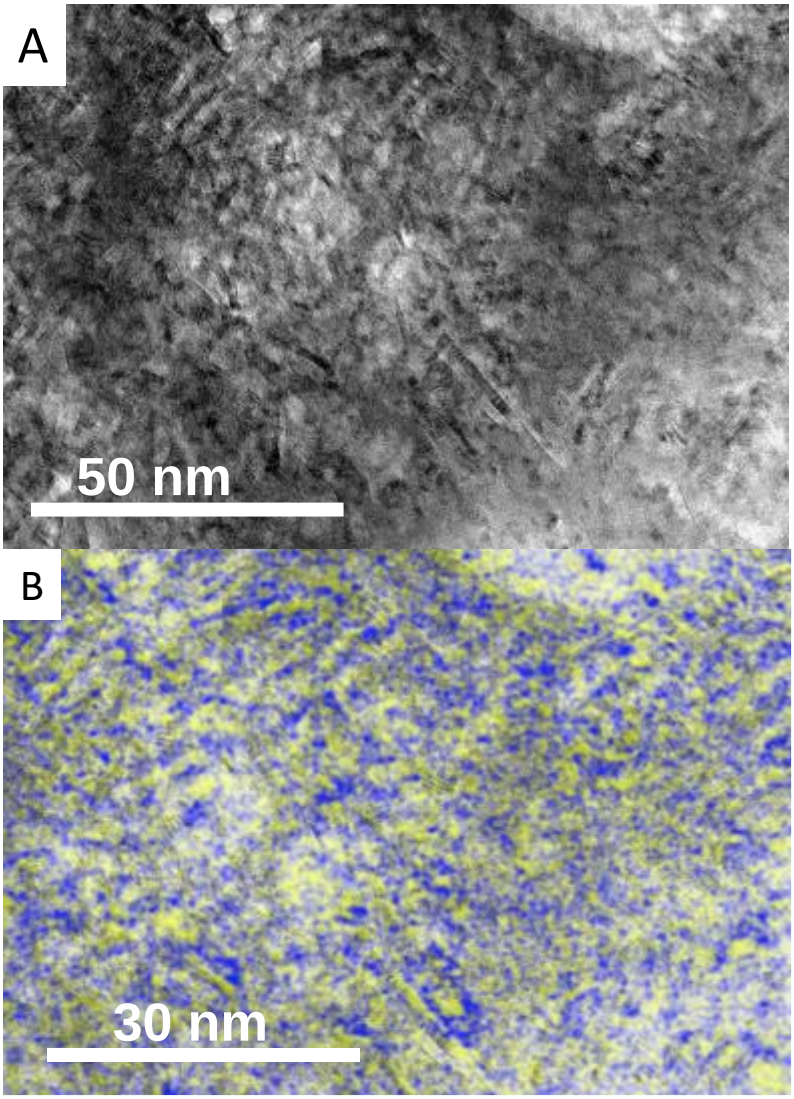

Fig. S5.

Energy Filtered TEM.

(A) TEM image of a sample from the brittlestar lens after heating for 30 min at 300°C so as to enlarge the nanoparticles. (B) Energy Filtered TEM of the same area with artificially added color. Blue: image produced with electrons that have the energy that fits that of Ca $L_{2,3}$-edge. Yellow: image produced with electrons that have the energy that fits that of Mg $L_{2,3}$-edge. It can be seen that the particles have a stronger yellow component as compared to areas of the matrix.

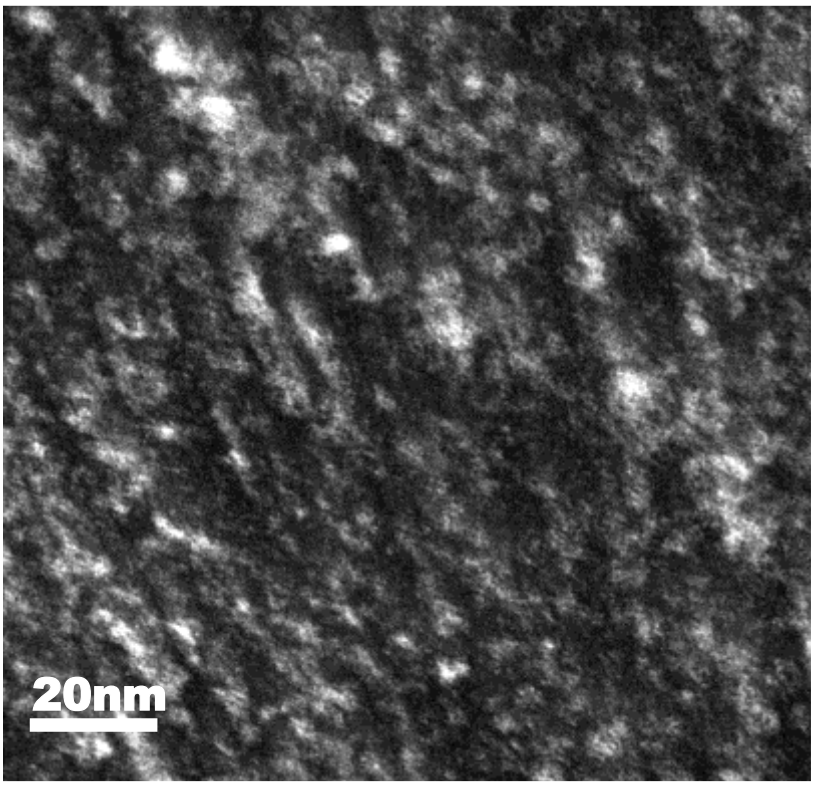

Fig. S6.

Dark field TEM image of a sample of the lens after heating at 500°C demonstrating absence of strain fringes as seen on same sample before the heat treatment (**Fig. 1E**).

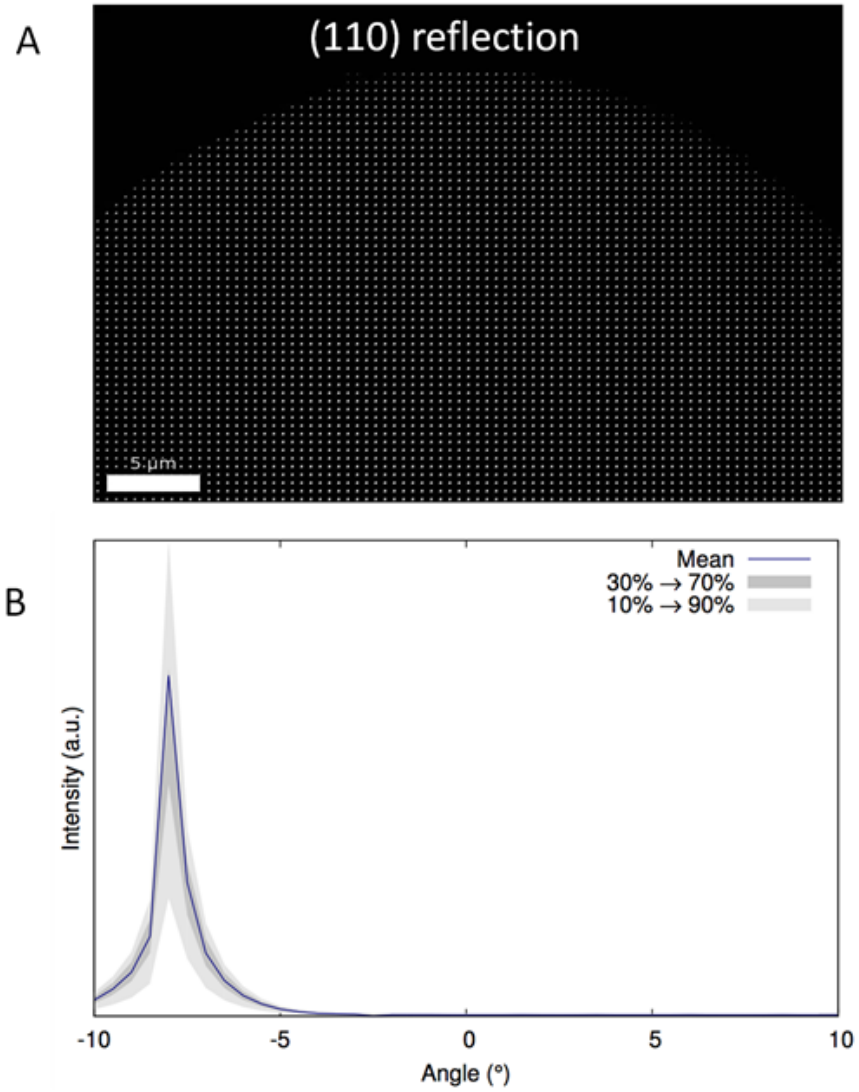

Fig. S7.

Scanning sub-micron synchrotron diffraction results for (110) reflection.
(A) Detailed analysis of a single lens using the (110) reflection. The area of the lens was scanned around the angle of maximum intensity: −7.85°. Although the diffraction spots vary in intensity, they are all at exactly the same position in the diffraction pattern. This finding indicates the sample's single-crystalline nature. (B) 2-D rocking curve for (110) reflection. Rocking curve is calculated from the single lens scan, showing a very sharp peak with a FWHM of only 0.1°.

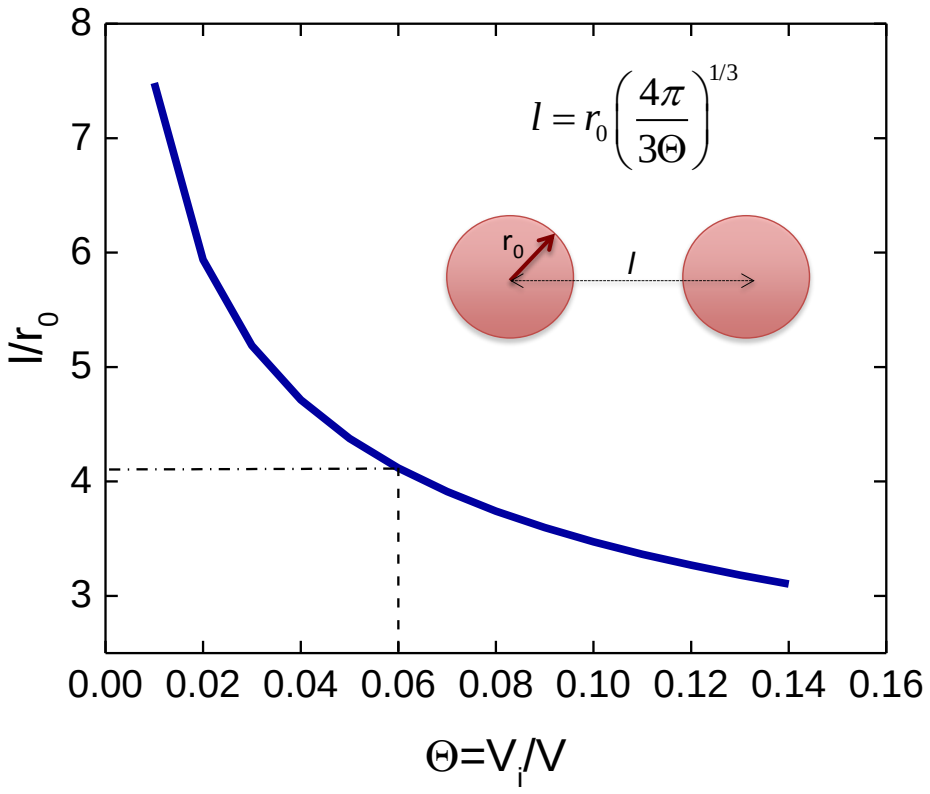

Fig. S8.

The average distance between inclusions as a function of their volume fraction. As can be seen from the plotted curve at a precipitate volume fraction of 6% the average distance between particle surfaces is only $2r_0$.

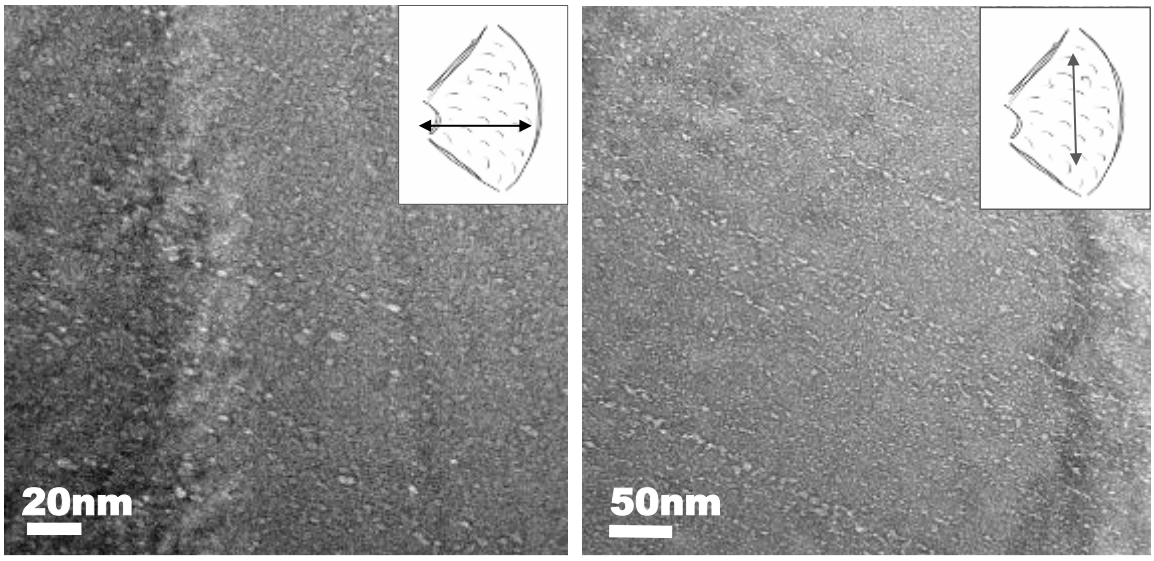

Fig. S9.
TEM imaging from different orientations indicating platelet-like shape of the nanoprecipitates.
TEM bright field mode images of the sample cut in horizontal direction (left) and vertical direction (right). As can be seen nanoprecipitates have more roundish shape when observed from horizontal direction and are more elongated when observed from vertical direction. The latter implies that nanoprecipitates are most likely nanoplatelets.

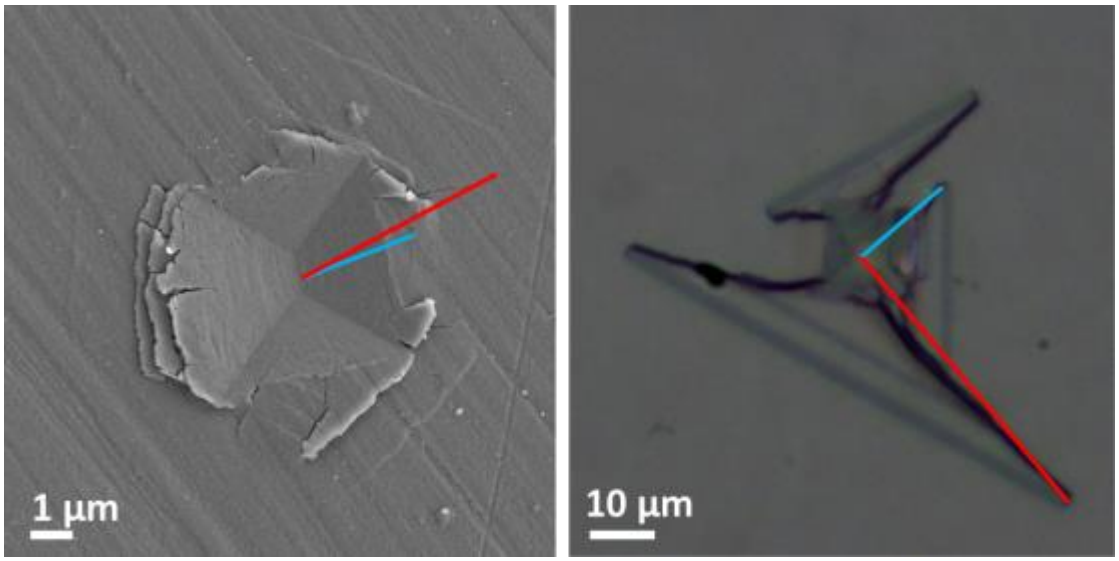

Fig. S10.
A representative microindentation experiment.
Representative images of indentations with corresponding crack size measurements (longest (red) and shortest(blue) of the cracks) for (001) in calcite from brittlestar lenses (left, scanning electron microscope image) and in geocalcite (001) (right, optical microscope image).

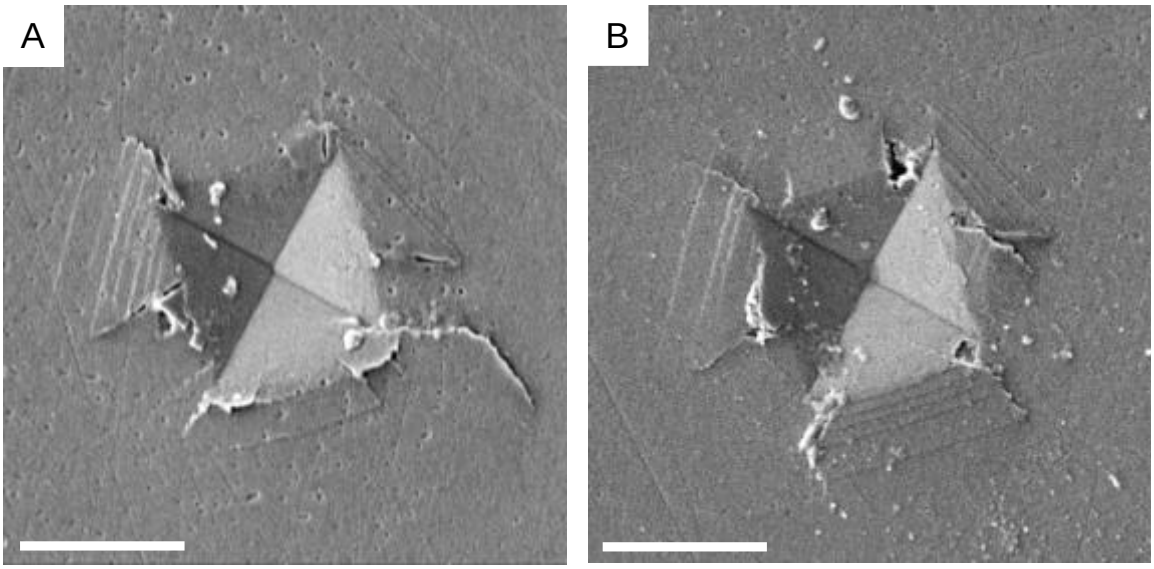

Fig. S11.
Microindentation experiments on the heat-treated lenses.
(A), (B) SEM images of indentations in the lenses annealed during 1h at 400°C. Scale bar is 5µm.

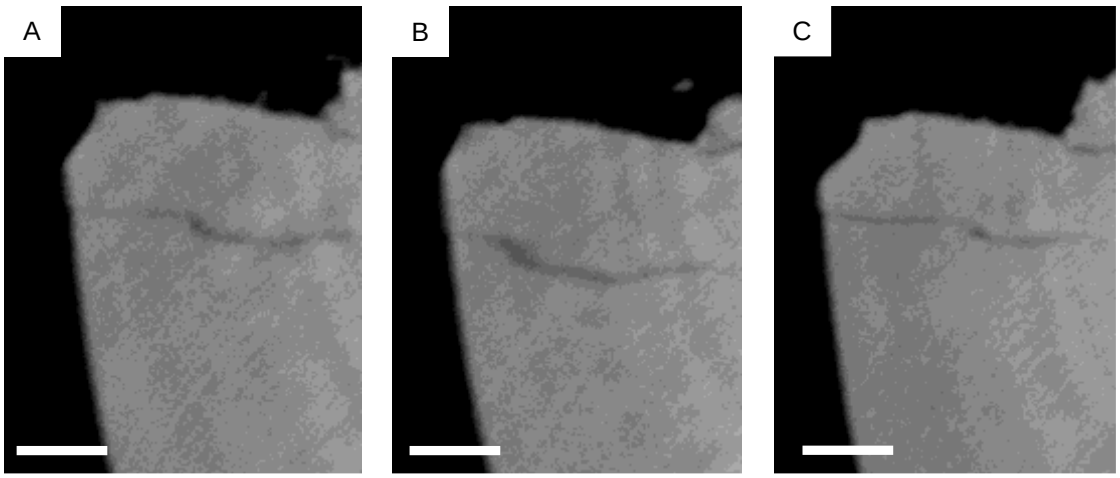

Fig. S12.
Crack deflection observed via nanoCT**.**
(A), (B) and (C) Nanotomographic maps obtained from different depths (B is 200nm deeper than A and C is 200nm deeper than B) demonstrating the deflection of a crack. Scale bar is 2µm.

Table S1.
Inductively Coupled Plasma Optical Emission Spectroscopy Results.

Exp. #	**Ca [mg]**	**Mg [mg]**	**Ca [#mol]**	**Mg [#mol]**	**CO_3**	**Calculated mol%$_{Mg}$(SD)**
1 **(per 10 ml)**	0.599513	0.066245	1.49E-05	2.72E-06	7.07E-05	15.41(9)
2 **(per 20 ml)**	1.216666	0.131140	3.04E-05	5.40E-06	1.43E-04	15.09(11)
3 **(per 20 ml)**	0.925466	0.099460	2.31E-05	4.09E-06	1.09E-04	15.05(7)
Average from the 3 experiments						**15.2(1)**

Table S2.
Electron Probe Micro-Analysis Results.

Sample	EPMA Mg ± SD (elemental wt%)	EPMA Mg ± SD (Mg at % cation per calcite CO_3 group equivalent to η=Mg/(Ca+Mg) mol%))	PEEM XANES spectra peak 2 position ± SD (eV)
Chihuahua Calcite	0.02 ± 0.05 wt %	0 ± 0 at %	537.35 ± 0.05 eV
***Ophiocoma* Lens low Mg-calcite**	—	—	537.30 ± 0.05 eV
***Ophiocoma* Lens averaged**	3.2 ± 0.3 wt %	13 ± 1 at %	537.60 ± 0.05 eV
***Ophiocoma* Lens high Mg-calcite**	—	—	537.80 ± 0.05 eV
Black Rock Dolomite	11.7 ± 0.2 wt %	45 ± 3 at %	537.96 ± 0.05 eV

Table S3.
Rietveld refinement results.
Extracted crystal lattice parameters, weight phase fractions at different temperatures and goodness of fit parameters.

Temp., °C	Phase name	Phase fraction, wt%	*a, b*-parameters, Å (ESDs)	*c*-parameter, Å (SD)	GOF	wR, %
RT	low-Mg $CaCO_3$	100	4.92577(3)	16.76897(6)	3.95	13.64
200	low-Mg $CaCO_3$	100	4.9263(6)	16.7769(1)	6.21	21.31
300	low-Mg $CaCO_3$	100	4.9289(13)	16.8332(3)	4.98	17.59
400	low-Mg $CaCO_3$ high-Mg $CaCO_3$	91.5 8.5	4.9488(44) 4.837(1)	16.918(1) 16.155(2)	2.33	8.06
450	low-Mg $CaCO_3$ high-Mg $CaCO_3$	89.4 10.6	4.9549(46) 4.838(1)	16.9420(11) 16.1614(3)	3.27	11.42
500	low-Mg $CaCO_3$ high-Mg $CaCO_3$	90.5 9.5	4.9561(42) 4.838(12)	16.943(1) 16.144(3)	3.35	11.89
550	low-Mg $CaCO_3$ high-Mg $CaCO_3$ MgO	91.1 8.4 0.5	4.9566(42) 4.837(12) 4.2169(2)	16.9409(99) 16.1378(31) 4.2169(17)	3.54	12.71
600	low-Mg $CaCO_3$ high-Mg $CaCO_3$ MgO	90.5 8 1.5	4.957 (4) 4.838(2) 4.2169(17)	16.9379(11) 16.138(4) 4.2169(2)	3.73	13.73
650	low-Mg $CaCO_3$ high-Mg $CaCO_3$ MgO	73.3 21 5.7	4.9859(27) 4.9552(58) 4.2169(17)	17.0957(5) 16.8981(14) 4.2169(17)	3.33	12.48

Table S4.

Estimated modulus and hardness values at different loads and loading rates. Obtained results are compared with the data of nanoindentation experiments using a Berkovich tip. The values were reported from the reference that corresponds to two different orientations (0^o, 60^o) of the threefold symmetric Berkovich tip relative to the calcite crystal during indentation**.**

Sample	**Number of indentations**	**Loading rate dP/dt (mN/min)**	**Maximum load P_{max} (mN)**	**Modulus ±SD E (GPa)**	**Hardness ±SD H (GPa)**
Lenses (001)	25	50	100	68.9±11.5	7.46±1.62
Geocalcite (001)	10	50	100	93.89±17.76	4.32±1.06
Heat-treated lenses (001)	20	50	100	36.13±2.8	3.52±1.02
For comparison[28]					
Biogenic calcite		30	2.5	70.1 ± 1.5 - 74.9 ± 0.7	3.47 ± 0.2 - 4.19 ± 0.3
Geocalcite (001)				67.5 ± 1.1 - 76.9 ± 3.1	2.30 ± 0.1 - 2.46 ± 0.03

Table S5.
The fracture toughness estimated from the measured mechanical properties.

Sample	Number of indentations used	Fracture toughness ±SD, (MPa.m ^{½}) K_{IC}	Fracture toughness ±SD, (MPa.m ^{½}) K_{IC}	Fracture toughness ±SD, (MPa.m ^{½}) K_{IC}
		Maximum crack length	**Minimum crack length**	**Average crack length**
Lenses (001)	8	0.34±0.08	0.51±0.14	0.42±0.08
Heat-treated lenses (001)	8	0.24±0.05	0.38±0.05	0.31±0.05
Geocalcite (001)	8	0.09±0.06	0.28±0.11	0.19±0.08

Movie S1

Directional SAXS maps of a lens

This movie maps the directional SAXS intensity over the area of the lens, as a function of its direction, with 0.25° increments. The periodicities of the SAXS signals are 2.5-16.5 nm. The rotating arrow (top left) indicates the direction in which the intensity in the corresponding frame is measured. The stripes which are parallel to the surface, and the surface area itself, have a highly directional SAXS signal. The direction of the max intensity in these regions is perpendicular to the surface. Also, some internal features with high directionality are seen.

References and Notes

1. A. H. Heuer, D. J. Fink, V. J. Laraia, J. L. Arias, P. D. Calvert, K. Kendall, G. L. Messing, J. Blackwell, P. C. Rieke, D. H. Thompson, et, Innovative materials processing strategies: A biomimetic approach. *Science* **255**, 1098–1105 (1992). doi:10.1126/science.1546311 Medline

2. L. M. Gordon, M. J. Cohen, K. W. MacRenaris, J. D. Pasteris, T. Seda, D. Joester, Dental materials. Amorphous intergranular phases control the properties of rodent tooth enamel. *Science* **347**, 746–750 (2015). doi:10.1126/science.1258950 Medline

3. J. A. Raven, A. H. Knoll, Non-skeletal biomineralization by eukaryotes: Matters of moment and gravity. *Geomicrobiol. J.* **27**, 572–584 (2010). doi:10.1080/01490451003702990

4. R. Blakemore, Magnetotactic bacteria. *Science* **190**, 377–379 (1975). doi:10.1126/science.170679 Medline

5. J. C. Weaver, G. W. Milliron, A. Miserez, K. Evans-Lutterodt, S. Herrera, I. Gallana, W. J. Mershon, B. Swanson, P. Zavattieri, E. DiMasi, D. Kisailus, The stomatopod dactyl club: A formidable damage-tolerant biological hammer. *Science* **336**, 1275–1280 (2012). doi:10.1126/science.1218764 Medline

6. V. C. Sundar, A. D. Yablon, J. L. Grazul, M. Ilan, J. Aizenberg, Fibre-optical features of a glass sponge. *Nature* **424**, 899–900 (2003). doi:10.1038/424899a Medline

7. L. Li, M. J. Connors, M. Kolle, G. T. England, D. I. Speiser, X. Xiao, J. Aizenberg, C. Ortiz, Multifunctionality of chiton biomineralized armor with an integrated visual system. *Science* **350**, 952–956 (2015). doi:10.1126/science.aad1246 Medline

8. A. Herman, L. Addadi, S. Weiner, Interactions of sea-urchin skeleton macromolecules with growing calcite crystals - a study of intracrystalline proteins. *Nature* **331**, 546–548 (1988). doi:10.1038/331546a0

9. P. Fratzl, R. Weinkamer, Nature's hierarchical materials. *Prog. Mater. Sci.* **52**, 1263–1334 (2007). doi:10.1016/j.pmatsci.2007.06.001

10. A. R. Studart, Biological and bioinspired composites with spatially tunable heterogeneous architectures. *Adv. Funct. Mater.* **23**, 4423–4436 (2013). doi:10.1002/adfm.201300340

11. E. Beniash, J. Aizenberg, L. Addadi, S. Weiner, Amorphous calcium carbonate transforms into calcite during sea urchin larval spicule growth. *Proc. R. Soc. London Ser. B* **264**, 461–465 (1997). doi:10.1098/rspb.1997.0066

12. Y. Politi, T. Arad, E. Klein, S. Weiner, L. Addadi, Sea urchin spine calcite forms via a transient amorphous calcium carbonate phase. *Science* **306**, 1161–1164 (2004). doi:10.1126/science.1102289 Medline

13. N. Vogel, S. Utech, G. T. England, T. Shirman, K. R. Phillips, N. Koay, I. B. Burgess, M. Kolle, D. A. Weitz, J. Aizenberg, Color from hierarchy: Diverse optical properties of micron-sized spherical colloidal assemblies. *Proc. Natl. Acad. Sci. U.S.A.* **112**, 10845–10850 (2015). doi:10.1073/pnas.1506272112 Medline

14. O. B. M. Hardouin Duparc, The Preston of the Guinier-Preston zones. Guinier. *Metall. Mater. Trans. A Phys. Metall. Mater. Sci.* **41**, 1873–1882 (2010). doi:10.1007/s11661-010-0320-5

15. Materials and methods and supplementary text are available as supplementary materials.

16. J. Aizenberg, A. Tkachenko, S. Weiner, L. Addadi, G. Hendler, Calcitic microlenses as part of the photoreceptor system in brittlestars. *Nature* **412**, 819–822 (2001). doi:10.1038/35090573 Medline

17. G. Hendler, M. Byrne, Fine structure of the dorsal arm plate of *Ophiocoma wendti*: Evidence for a photoreceptor system (Echinodermata, Ophiuroidea). *Zoomorphology* **107**, 261–272 (1987). doi:10.1007/BF00312172

18. E. Zolotoyabko, E. N. Caspi, J. S. Fieramosca, R. B. Von Dreele, F. Marin, G. Mor, L. Addadi, S. Weiner, Y. Politi, Differences between bond lengths in biogenic and geological calcite. *Cryst. Growth Des.* **10**, 1207–1214 (2010). doi:10.1021/cg901195t

19. B. Pokroy, A. N. Fitch, F. Marin, M. Kapon, N. Adir, E. Zolotoyabko, Anisotropic lattice distortions in biogenic calcite induced by intra-crystalline organic molecules. *J. Struct. Biol.* **155**, 96–103 (2006). doi:10.1016/j.jsb.2006.03.008 Medline

20. R. I. Harker, O. F. Tuttle, Studies in the system CaO-MgO-CO_2; Part 2, Limits of solid solution along the binary join $CaCO_3$-$MgCO_3$. *Am. J. Sci.* **253**, 274–282 (1955). doi:10.2475/ajs.253.5.274

21. P. Fratzl, O. Penrose, J. L. Lebowitz, Modeling of phase separation in alloys with coherent elastic misfit. *J. Stat. Phys.* **95**, 1429–1503 (1999). doi:10.1023/A:1004587425006

22. T. Mori, K. Tanaka, Average stress in matrix and average elastic energy of materials with misfitting inclusions. *Acta Metall.* **21**, 571–574 (1973). doi:10.1016/0001-6160(73)90064-3

23. B. Pokroy, E. Zolotoyabko, Aragonite growth on single-crystal substrates displaying a threefold axis. *Chem. Commun. (Camb.)* **16**, 2140–2142 (2005). doi:10.1039/b500584a Medline

24. P. N. T. Unwin, G. W. Lorimer, R. B. Nicholson, The origin of the grain boundary precipitate free zone. *Acta Metall.* **17**, 1363–1377 (1969). doi:10.1016/0001-6160(69)90154-0

25. S. M. Wise, J. S. Kim, W. C. Johnson, Surface-directed spinodal decomposition in a stressed, two-dimensional, thin film. *Thin Solid Films* **473**, 151–163 (2005). doi:10.1016/j.tsf.2004.07.075

26. B. Aichmayer, P. Fratzl, S. Puri, G. Saller, Surface-directed spinodal decomposition on a macroscopic scale in a nitrogen and carbon alloyed steel. *Phys. Rev. Lett.* **91**, 015701 (2003). doi:10.1103/PhysRevLett.91.015701 Medline

27. B. Lawn, R. Wilshaw, Indentation fracture - principles and applications. *J. Mater. Sci.* **10**, 1049–1081 (1975). doi:10.1007/BF00823224

28. A. G. Evans, E. A. Charles; A. G. Evans, E. A. Charles, Fracture toughness determinations by indentation. *J. Am. Ceram. Soc.* **59**, 371–372 (1976). doi:10.1111/j.1151-2916.1976.tb10991.x

29. M. E. Kunitake, L. M. Mangano, J. M. Peloquin, S. P. Baker, L. A. Estroff, Evaluation of strengthening mechanisms in calcite single crystals from mollusk shells. *Acta Biomater.* **9**, 5353–5359 (2013). doi:10.1016/j.actbio.2012.09.030 Medline

30. O. Kolednik, J. Predan, F. D. Fischer, P. Fratzl, Bioinspired design criteria for damage-resistant materials with periodically varying microstructure. *Adv. Funct. Mater.* **21**, 3634–3641 (2011). doi:10.1002/adfm.201100443

31. D. Grady, R. Hollenbach, Dynamic fracture strength of rock. *Geophys. Res. Lett.* **6**, 73–76 (1979). doi:10.1029/GL006i002p00073

32. B. Pokroy, V. Demensky, E. Zolotoyabko, Nacre in mollusk shells as a multilayered structure with strain gradient. *Adv. Funct. Mater.* **19**, 1054–1059 (2009). doi:10.1002/adfm.200801201

33. J. B. Forien, C. Fleck, P. Cloetens, G. Duda, P. Fratzl, E. Zolotoyabko, P. Zaslansky, Compressive residual strains in mineral nanoparticles as a possible origin of enhanced crack resistance in human tooth dentin. *Nano Lett.* **15**, 3729–3734 (2015). doi:10.1021/acs.nanolett.5b00143 Medline

34. B. H. Toby, R. B. Von Dreele, GSAS-II: The genesis of a modern open-source all purpose crystallography software package. *J. Appl. Cryst.* **46**, 544–549 (2013). doi:10.1107/S0021889813003531

35. R. T. DeVol, C.-Y. Sun, M. A. Marcus, S. N. Coppersmith, S. C. B. Myneni, P. U. P. A. Gilbert, Nanoscale transforming mineral phases in fresh nacre. *J. Am. Chem. Soc.* **137**, 13325–13333 (2015). doi:10.1021/jacs.5b07931 Medline

36. Y. U. T. Gong, C. E. Killian, I. C. Olson, N. P. Appathurai, A. L. Amasino, M. C. Martin, L. J. Holt, F. H. Wilt, P. U. P. A. Gilbert, Phase transitions in biogenic amorphous calcium carbonate. *Proc. Natl. Acad. Sci. U.S.A.* **109**, 6088–6093 (2012). doi:10.1073/pnas.1118085109 Medline

37. GG–Macros, http://home.physics.wisc.edu/gilbert/software.htm, (2016).

38. R. A. Metzler, G. A. Tribello, M. Parrinello, P. U. P. A. Gilbert, Asprich peptides are occluded in calcite and permanently disorder biomineral crystals. *J. Am. Chem. Soc.* **132**, 11585–11591 (2010). doi:10.1021/ja103089r Medline

39. G. De Stasio, B. H. Frazer, B. Gilbert, K. L. Richter, J. W. Valley, Compensation of charging in X-PEEM: A successful test on mineral inclusions in 4.4 Ga old zircon. *Ultramicroscopy* **98**, 57–62 (2003). doi:10.1016/S0304-3991(03)00088-3 Medline

40. M. A. Marcus, A. A. MacDowell, R. Celestre, A. Manceau, T. Miller, H. A. Padmore, R. E. Sublett, Beamline 10.3.2 at ALS: A hard x-ray microprobe for environmental and materials sciences. *J. Synchrotron Radiat.* **11**, 239–247 (2004). doi:10.1107/S0909049504005837 Medline

41. P. Pfalzer, J.-P. Urbach, M. Klemm, S. Horn, M. L. denBoer, A. I. Frenkel, J. P. Kirkland, Elimination of self-absorption in fluorescence hard-x-ray absorption spectra. *Phys. Rev. B* **60**, 9335–9339 (1999). doi:10.1103/PhysRevB.60.9335

42. R. T. DeVol, R. A. Metzler, L. Kabalah-Amitai, B. Pokroy, Y. Politi, A. Gal, L. Addadi, S. Weiner, A. Fernandez-Martinez, R. Demichelis, J. D. Gale, J. Ihli, F. C. Meldrum, A. Z. Blonsky, C. E. Killian, C. B. Salling, A. T. Young, M. A. Marcus, A. Scholl, A. Doran, C. Jenkins, H. A. Bechtel, P. U. P. A. Gilbert, Oxygen spectroscopy and polarization-dependent imaging contrast (PIC)-mapping of calcium carbonate minerals and biominerals. *J. Phys. Chem. B* **118**, 8449–8457 (2014). doi:10.1021/jp503700g Medline

43. B. Ravel, M. Newville, Athena, Artemis, Hephaestus: Data analysis for x-ray absorption spectroscopy using IFEFFIT. *J. Synchrotron Radiat.* **12**, 537–541 (2005). doi:10.1107/S0909049505012719 Medline

44. W. C. Oliver, G. M. Pharr, An improved technique for determining hardness and elastic modulus using load and displacement sensing indentation experiments. *J. Mater. Res.* **7**, 1564–1583 (1992). doi:10.1557/JMR.1992.1564

45. W. C. Oliver, G. M. Pharr, Measurement of hardness and elastic modulus by instrumented indentation: Advances in understanding and refinements to methodology. *J. Mater. Res.* **19**, 3–20 (2004). doi:10.1557/jmr.2004.19.1.3

46. G. Martínez-Criado, J. Villanova, R. Tucoulou, D. Salomon, J.-P. Suuronen, S. Labouré, C. Guilloud, V. Valls, R. Barrett, E. Gagliardini, Y. Dabin, R. Baker, S. Bohic, C. Cohen, J. Morse, ID16B: A hard x-ray nanoprobe beamline at the ESRF for nano-analysis. *J. Synchrotron Radiat.* **23**, 344–352 (2016). doi:10.1107/S1600577515019839 Medline

47. P. Cloetens, W. Ludwig, J. Baruchel, D. Van Dyck, J. Van Landuyt, J. P. Guigay, M. Schlenker, Holotomography: Quantitative phase tomography with micrometer resolution using hard synchrotron radiation x rays. *Appl. Phys. Lett.* **75**, 2912–2914 (1999). doi:10.1063/1.125225

48. J. Schindelin, I. Arganda-Carreras, E. Frise, V. Kaynig, M. Longair, T. Pietzsch, S. Preibisch, C. Rueden, S. Saalfeld, B. Schmid, J.-Y. Tinevez, D. J. White, V. Hartenstein, K. Eliceiri, P. Tomancak, A. Cardona, Fiji: An open-source platform for biological-image analysis. *Nat. Methods* **9**, 676–682 (2012). doi:10.1038/nmeth.2019 Medline

49. J. W. Morris Jr., The Khachaturyan theory of elastic inclusions: Recollections and results. *Philos. Mag.* **90**, 3–35 (2010). doi:10.1080/14786430902934256

50. T. Mura, Kluwer Academic Publisher, Dordrecht, 1987.

51. C.-C. Chen, C.-C. Lin, L.-G. Liu, S. V. Sinogeikin, J. D. Bass, Elasticity of single-crystal calcite and rhodochrosite by Brillouin spectroscopy. *Am. Mineral.* **86**, 1525–1529 (2001). doi:10.2138/am-2001-11-1222

52. A. Masic, J. C. Weaver, Large area sub-micron chemical imaging of magnesium in sea urchin teeth. *J. Struct. Biol.* **189**, 269–275 (2015). doi:10.1016/j.jsb.2014.12.005 Medline

53. B. Pokroy, A. N. Fitch, P. L. Lee, J. P. Quintana, E. N. Caspi, E. Zolotoyabko, Anisotropic lattice distortions in the mollusk-made aragonite: A widespread phenomenon. *J. Struct. Biol.* **153**, 145–150 (2006). doi:10.1016/j.jsb.2005.10.009 Medline

54. T. Williams, C. Kelley, *Gnuplot 5.0: reference manual*. ([sn], 2015).

ALSO IN *SCIENCE* JOURNALS

Edited by **Stella Hurtley**

PALEOANTHROPOLOGY

The peopling of Asia

In recent years, there has been increasing focus on the paleoanthropology of Asia, particularly the migration patterns of early modern humans as they spread out of Africa. Bae *et al*. review the current state of the Late Pleistocene Asian human evolutionary record from archaeology, hominin paleontology, geochronology, genetics, and paleoclimatology. They evaluate single versus multiple dispersal models and southern versus the northern dispersal routes across the Asian continent. They also review behavioral and environmental variability and how these may have affected modern human dispersals and interactions with indigenous populations. —AMS

Science, this issue p. 1269

SUSTAINABILITY

Optimizing flow in dammed rivers

Hydropower dams radically alter river flow regimes, often with consequences for the functioning and productivity of the waters downstream. Where fisheries in large tropical river systems are affected, there can be knock-on effects on food security. For the Mekong River, Sabo *et al*. used a data-based time series modeling approach to estimate the features of the flow regime that optimize the fishery that is crucial to food security in Cambodia (see the Perspective by Poff and Olden). Fish futures can be maximized within a managed hydrologic system with careful prescription of flows. Such data-driven approaches can be used to link hydrology to ecology and food production and specify design principles that could help to deliver food security in other river systems. —AMS

Science, this issue p. 1270; see also p. 1252

MACHINE LEARNING

Computer or human?

Proving that we are human is now part of many tasks that we do on the internet, such as creating an email account, voting in an online poll, or even downloading a scientific paper. One of the most popular tests is text-based CAPTCHA, where would-be users are asked to decipher letters that may be distorted, partially obscured, or shown against a busy background. This test is used because computers find it tricky, but (most) humans do not. George *et al*. developed a hierarchical model for computer vision that was able to solve CAPTCHAs with a high accuracy rate using comparatively little training data. The results suggest that moving away from text-based CAPTCHAs, as some online services have done, may be a good idea. —JS

Science, this issue p. 1271

SOLID-STATE PHYSICS

Probing an excitonic condensate

Excitons—bound states of electrons and holes in solids—are expected to form a Bose condensate at sufficiently low temperatures. Excitonic condensation has been studied in systems such as quantum Hall bilayers where physical separation between electrons and holes enables a longer lifetime for their bound states. Kogar *et al*. observed excitons condensing in the three-dimensional semimetal 1*T*-$TiSe_2$. In such systems, distinguishing exciton condensation from other types of order is tricky. To do so, the authors used momentum-resolved electron energy-loss spectroscopy, a technique developed to probe electronic collective excitations. The energy needed to excite an electronic mode became negligible at a finite momentum, signifying the formation of a condensate. —JS

Science, this issue p. 1314

NEURODEVELOPMENT

Building a brain

The human brain is built in an inside-out manner as a series of layers. Although progenitor cells spin off new neurons in a seemingly organized fashion, the devil is in the details. Nowakowski *et al*. analyzed the transcriptomes of single cells from the developing brain to elucidate the hidden complexity of brain construction. For each cell, its position within the brain matters, as well as what type of neuron is being made at what point during overall development. These individual expression patterns result in organized diversity in the brain's cortex. —PJH

Science, this issue p. 1318

TOPOLOGICAL MATTER

A magnetic tip reconfigures edge states

Topological phases of matter are characterized by invariants such as Chern numbers, which determine their global properties. On the boundary of two domains with different Chern numbers, chiral edge states are expected to form. Yasuda *et al*. engineered such states in samples of a quantum anomalous Hall material by creating magnetic domains using the tip of a magnetic force microscope. The existence of chiral edge states along the domain walls was confirmed with electrical transport measurements. The ability to reconfigure and manipulate these states may improve spintronics. —JS

Science, this issue p. 1311

BIOCHEMISTRY

A biotech tour de force

RuBisCo, the key enzyme of photosynthesis, is a complex of eight large and eight small subunits. It mediates the fixation of atmospheric CO_2 in the Calvin-Benson-Bassham cycle. In addition to being enzymatically inefficient, RuBisCo has a problem with distinguishing between CO_2 and O_2. The fixation of O_2 results in the energetically wasteful reaction of photorespiration. Thus, there is a strong incentive to improve RuBisCo's catalytic properties by engineering. However, for decades, it has been impossible to express the enzyme from plants in an easily manipulatable bacterial host. Aigner *et al*. succeeded in functionally expressing plant RuBisCo in *Escherichia coli* (see the Perspective by Yeates and Wheatley). This should allow for the systematic mutational analysis of RuBisCo and selection of favorable variants for improved crop yields. —SMH

Science, this issue p. 1272; see also p. 1253

CHEMICAL PHYSICS

Clocking departures from chiral origins

Just as the atoms in a molecule can be arranged in a left- or right-handed manner, the field in a beam of light can circulate like a left- or right-handed corkscrew. Matches or mismatches in this mutual handedness give rise to an asymmetric distribution of trajectories as electrons are ejected during photoionization. Beaulieu *et al*. used an interferometric approach to uncover the temporal dynamics associated with this asymmetry. They probed the mirror-image isomers of camphor with circularly polarized light, which revealed the angle-dependent delays between trajectories that spanned up to 24 attoseconds. —JSY

Science, this issue p. 1288

BIOLOGICAL MATERIALS

Many roads to being tough

A number of routes exist to increase toughness in both natural and human-made materials—for example, using

secondary phases and precipitates or exploiting tailored architectures and shaped crystals. Polishchuk *et al*. detail the nanoscale internal structure of calcitic microlenses formed by a brittlestar (see the Perspective by Duffy). The segregation of magnesium-rich particles forms a secondary phase that places compressive stresses on the host matrix. This toughening mechanism resembles Guinier–Preston zones known in classical metallurgy. —MSL

Science, this issue p. 1294
see also p. 1254

STRUCTURAL BIOLOGY

A source of methane in the upper ocean

Methane concentrations are high in oxygenated surface waters. Methylphosphonate (MPn) is a suggested source, but an enzyme that synthesizes Mpn (MPnS) has so far only been identified in one ocean microbe, albeit an abundant one: the archaeon *Nitrosopumilus maritimus*. Born *et al*. describe the crystal structure of MPnS and of a related enzyme that acts on the same substrate but makes a different product. By comparing the structures, they determined sequence markers that allowed them to identify MPnS in other ocean microbes, including the abundant microbe *Pelagibacter ubique*. These findings support the proposal that MPn is a source of both methane and phosphorus in the upper aerobic ocean. —VV

Science, this issue p. 1336

ATMOSPHERE

An even longer road to recovery?

The ozone layer is on the path to recovery after concerted efforts to control the production of ozone-depleting substances under the Montreal Protocol. In the latter half of the 21st century, the ozone layer will be controlled mainly by atmospheric carbon dioxide concentrations. In a Perspective, Liang *et al.* explain that ozone layer recovery may slow down. This is because of incomplete compliance with the Montreal Protocol, rising emissions of ozone-depleting substances that are not controlled, and increasing emissions of natural ozone-destroying substances owing to climate change. Full recovery of the ozone layer to its 1980 state will require improved compliance with regulations and successful efforts to limit climate change. —JFU

Science, this issue p. 1257

DENDRITIC CELLS

Priming T follicular helper cells

In our immune systems, T follicular helper (Tfh) cells modulate antibody production by B cells. Krishnaswamy *et al.* examined the ability of conventional dendritic cell (cDC) subsets to prime Tfh commitment in response to intranasal immunization in mice. $CD11b^+$ migratory type 2 cDCs (cDC2s) played an essential role in promoting commitment of activated T cells to the Tfh lineage. The authors imaged trafficking of cDC2s after intranasal immunization and found that they carried antigens to the site within the lymph node where Tfh cell priming occurs. These findings have important implications for vaccine design and delivery. —AB

Sci. Immunol. **2**, eaam9169 (2017).

BONE

Detecting skeletal growth

During development, bone is created by a process called endochondral ossification, which results in the production of a fragment of type X collagen. Endochondral ossification also occurs during long bone growth and fracture healing. Coghlan *et al.* discovered that the type X collagen fragment could be isolated from blood and that its concentration correlated with skeletal growth velocity. Fragment concentration was inversely correlated with age and fluctuated during fracture healing in adults. The assay to quantify the fragment could be useful as a real-time marker of skeletal growth in children or for monitoring response to treatment for growth and bone disorders. —CC

Sci. Transl. Med. **9**, eaan4669 (2017).

RAF1, suggesting that their roles are not entirely overlapping. Much insight is provided into the BSD2 assembly chaperone, which contains a DnaJ-like zinc-binding cysteine-rich domain (*8*). A crystal structure of eight RuBisCO large subunits and eight BSD2 subunits appears to represent a stable late-stage intermediate in assembly; final displacement of the BSD2 subunits by RuBisCO small subunits completes the process. Intriguingly, the sites on the L_8 structure where BSD2 subunits bind and the sites where the small subunits finally sit are almost nonoverlapping; it appears that subtle conformational changes and steric effects couple the addition of small subunits to the departure of BSD2 subunits (see the figure).

Although Aigner *et al*. clarify much about the RuBisCO chaperone process (and how to implement it in bacteria for practical applications), some mysteries remain. The importance of RAF2 in assembling plant RuBisCO was confirmed, supporting earlier work in maize (*9*). But its mode of operation is still not clear. A recent structure of the cyanobacterial homolog of RAF2 (acRAF) showed it to be a defunct relic of a pterin dehydratase enzyme, which evolved a new function as a chaperone (*10*). Among the specialized RuBisCO assembly chaperones, RAF2 is now the only one for which no three-dimensional structural data are available when bound to RuBisCO subunits or peptide fragments, leaving open its mechanism of action. The roles of other endogenous *E. coli* chaperones, DnaK, DnaJ, and GrpE (*13*), were not evaluated in Aigner *et al*.'s work, leaving open the possibility of their additional contribution to plant RuBisCO assembly.

The *E. coli* RuBisCO assembly assay provides a facile experimental system to tease apart the functions and evolution of RuBisCO chaperones. For instance, why has RuBisCO seemingly acquired more folding and assembly chaperones as it evolved? Can plant RuBisCO be engineered more easily now to make an improved enzyme for agricultural use? A recent finding suggests that some of the chaperones might have special regulatory roles beyond assembly, including degradation of RuBisCO under particular stress conditions, such as starvation, to provide amino acids (*14*, *15*). RuBisCO is degraded to provide amino acids to cells during stress conditions and senescence (*12*). Could some of these chaperones, given their role in RuBisCO assembly, consequently regulate RuBisCO degradation as well? RuBisCO researchers can now answer these and other questions about the molecular evolution and detailed mechanisms of chaperoning and assembly of RuBisCO, one of the most important enzymes on Earth. ■

REFERENCES

1. S. G. Wildman, *Photosynth. Res.* **73**, 243 (2002).
2. I. Andersson, A. Backlund, *Plant Physiol. Biochem.* **46**, 275 (2008).
3. H. Aigner *et al.*, *Science* **358**, 1272 (2017).
4. B. Bukau, J. Weissman, A. Horwich, *Cell* **125**, 443 (2006).
5. M. Hayer-Hartl, A. Bracher, F. U. Hartl, *Trends Biochem. Sci.* **41**, 62 (2016).
6. S. Saschenbrecker *et al.*, *Cell* **129**, 1189 (2007).
7. T. Hauser *et al.*, *Nat. Struct. Mol. Biol.* **22**, 720 (2015).
8. T. P. Brutnell *et al.*, *Plant Cell* **11**, 849 (1999).
9. L. Feiz *et al.*, *Plant J.* **80**, 862 (2014).
10. N. M. Wheatley *et al.*, *J. Biol. Chem.* **289**, 7973 (2014).
11. P. Goloubinoff *et al.*, *Nature* **342**, 884 (1989).
12. L. P. Cloney *et al.*, *J. Biol. Chem.* **267**, 23333 (1992).
13. S. K. Checa, A. M. Viale, *FEBS J.* **248**, 848 (1997).
14. P. Kolesinski, M. Rydzy, A. Szczepaniak, *Photosynth. Res.* **132**, 135 (2017).
15. Y. Kato *et al.*, *Planta* **220**, 97 (2004).

10.1126/science.aar3107

RuBisCO assembly

Numerous plant chaperone genes were inserted into bacterial cells to promote the folding and assembly of the plant RuBisCO enzyme inside *E. coli*.

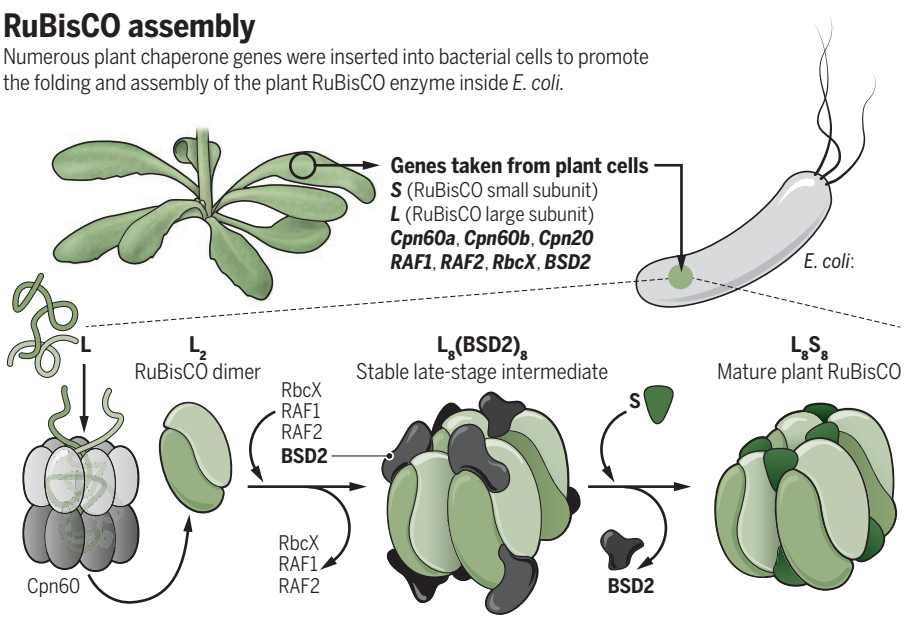

BIOLOGICAL MATERIALS

Coherent nanoparticles in calcite

A toughening strategy known to metallurgists is also used by the brittlestar

By **Dorothy M. Duffy**

Living organisms use a wide range of minerals to perform a variety of functions, including familiar examples such as bones (for support), teeth (for mastication), and shells (for protection), as well as other less common functions, such as optical, magnetic, and gravity sensing. These biominerals are produced with elements that are present in the local environment under ambient conditions. The ability to mimic biological strategies to improve current materials and processing methods is a long-standing goal of material scientists. On page 1294 of this issue, Polishchuk *et al*. (*1*) characterized the properties of a biomineral in the skeleton of the brittlestar, *Ophiocoma wendtii*. An array of microlenses on their skeletons focus light onto an optical receptor, enabling them to detect shadows and hide from predators. Nanoprecipitates in these lenses also toughen the skeleton, an effect that is achieved in engineered metal alloys only through expensive heat treatments.

The lenses are made of single-crystal calcite, ~50 μm in size, arranged in a hexagonal pattern on their dorsal arm plates. The microstructure of these brittlestar lenses has been known since 2002 (*2*), but until now, little was known about the nanostructure. Polishchuk *et al*. found that the single-crystal calcite lenses contained arrays of calcite nanoprecipitates, ~5 nm in diameter, that have a higher magnesium content than the host crystal. Further investigation revealed that these nanoprecipitates were coherent with the host, meaning that the crystal lattice planes were continuous as they passed through the nanoparticles. Coherent nanoparticles, sometimes referred to as Guinier–Preston, or GP, zones (*3*, *4*), are well known in metallurgy, where they are

Department of Physics and Astronomy and London Centre for Nanotechnology, University College London, Gower Street, London WC1E 6BT, UK. Email: d.duffy@ucl.ac.uk

GRAPHIC: K. SUTLIFF/*SCIENCE*

used to increase the strength of the metal. The presence of GP zones had not previously been detected in biominerals.

The microlenses of the brittlestar have a dual function. Not only do they focus light onto a receptor, but they are also part of the skeleton and, as such, they need to have robust mechanical properties. Like all minerals, calcite is very brittle, and it is susceptible to fracture. Organisms have developed a number of strategies to increase the toughness of biominerals. One of the most common, used in both bone (*5*) and seashells (*6, 7*), is the formation of complex hierarchical structures of hard and soft materials (*8*). The combination of hard and soft material is also used in synthetic composites, such as the carbon-fiber–reinforced polymers that have numerous high-strength, low-density applications.

Such complex structures would not be suitable for optical lenses, so these brittlestars required an alternative toughening strategy. The similarity of the magnesium-rich nanoparticles in the calcitic lenses to coherent nanoparticles in metals suggests that they may play a role in the enhancement of the mechanical properties. In metals, GP zones increase the tensile strength by inhibiting dislocation motion, but they also decrease ductility (increase brittleness) by the same mechanism.

Failure of brittle materials, such as calcite, occurs via a different mechanism than in metals, as dislocation mobility is limited. Brittle materials break catastrophically when a combination of the applied stress and the crack length reaches a critical value, known as the fracture toughness. The fracture toughness of a material is a measure of its resistance to fracture and is related to the energy required to extend existing cracks in a material. Fracture toughness can be increased by introducing interfaces to the material, as in bones, shells, and synthetic composites. It can also be increased by introducing a compressive stress, to counteract the applied tensile stress. Synthetic brittle materials that use such a strengthening mechanism include tempered glass and prestressed concrete.

The hypothesis put forward by Polishchuk *et al.* is that the magnesium-rich nanoparticles induce a compressive stress in the host calcite material, which increases the fracture toughness. The stress originates from the smaller lattice parameters of magnesium-rich calcite and the coherent nature of the lattice planes, which together create a tensile stress in the particles and a compensating compressive stress in the surrounding host crystal (see the figure). The hypothesis is supported by measurements of fracture toughness, which was found to be on the order of a factor of 2 higher than for single-crystal geological calcite.

Coherent nanoparticles in metals, such as aluminum, are formed by cooling a molten mixture of aluminum and copper to produce a supersaturated solid solution of copper atoms in aluminum (*9*). The solid solution is then heated, or annealed, and nanoparticles of a second phase, which have a high concentration of copper atoms, precipitate from the solid solution. The size of nanoparticles is controlled by the annealing temperature, as growth is limited by the rate at which the copper atoms diffuse through the crystal.

Biominerals must form under ambient conditions, and many biominerals are known to form from an amorphous precursor. As the solubility of magnesium in amorphous calcium carbonate is high, this precursor may be rich in magnesium. Magnesium is much less soluble in crystalline calcite than in amorphous calcium carbonate, so crystallization results in a supersaturated solid solution. Over time, the excess magnesium atoms diffuse to form coherent magnesium-rich precipitates. Such a formation mechanism of coherent nanoparticles in calcite is analogous to that of copper-rich nanoparticles in aluminum, as both evolve from supersaturated solid solutions.

Polishchuk *et al.* identified a toughening mechanism that does not disrupt the primary function of the biomineral—that is, the focusing of light. It is possible that prestressing by coherent nanoparticles occurs in other dual-function biominerals, where toughening with hierarchical structures is not an option, as it would disrupt the primary function of the biomineral. Future investigations should explore other dual-function biominerals to determine the extent to which nature employs such a strategy. Future research should also attempt to replicate the formation of coherent nanoparticles in minerals or ceramics by crystallization from an amorphous precursor, with the aim of developing an energy-efficient process for increasing the fracture toughness of ceramic materials. ■

Coherently embedding single nanoparticles

Polishchuk *et al.* show that the microlenses of the brittlestar contain magnesium (Mg)-rich nanoparticles. The lattice planes of the calcite skeleton bend near the particles to accommodate the smaller lattice vectors of the Mg-rich particle. The resulting compressive stress inhibits crack advancement and toughens the skeleton.

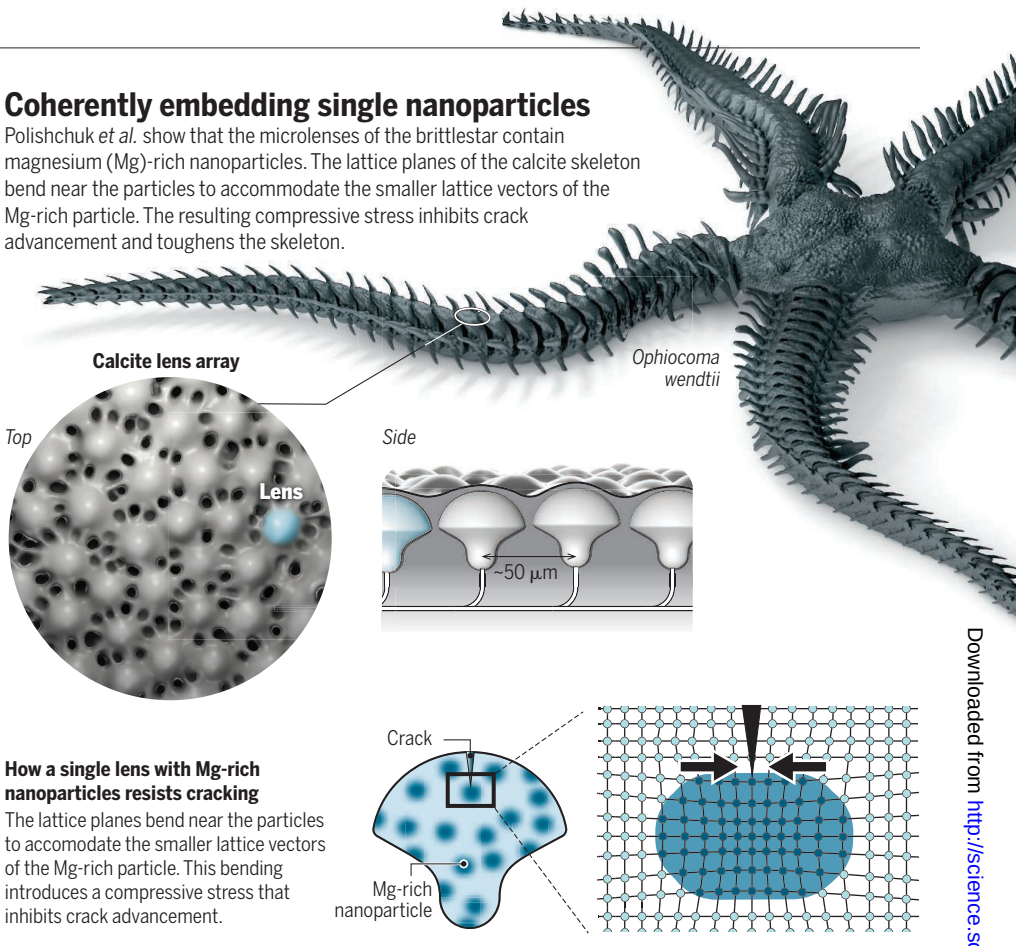

How a single lens with Mg-rich nanoparticles resists cracking
The lattice planes bend near the particles to accomodate the smaller lattice vectors of the Mg-rich particle. This bending introduces a compressive stress that inhibits crack advancement.

GRAPHIC: V. ALTOUNIAN/*SCIENCE*

REFERENCES

1. I. Polishchuk *et al.*, *Science* **358**, 1294 (2017).
2. J. Aizenberg, A. Tkachenko, S. Weiner, L. Addadi, G. Hendler, *Nature* **412**, 819 (2001).
3. A. Guinier, *Nature* **142**, 569 (1938).
4. G. D. Preston, *Proc. R. Soc. A* **167**, 526 (1938).
5. S. Weiner, H. D. Wagner, *Annu. Rev. Mater. Sci.* **28**, 271 (1998).
6. J. D. Currey, *Proc. R. Soc. B* **196**, 443 (1977).
7. F. Barthelat, H. Tang, P. D. Zavattieri, C.-M. Li, H. D. Espinosa, *J. Mech. Phys. Solids* **55**, 306 (2007).
8. P. Fratzl, R. Weinkamer, *Prog. Mater. Sci.* **52**, 1263 (2007).
9. S. P. Ringer, K. Hono, *Mater. Charact.* **44**, 101 (2000).

10.1126/science.aaq0111